Advances in Nano Research, *Vol. 16, No.6 (2024) 623-638*
https://doi.org/10.12989/anr.2024.16.6.623

Thermal post-buckling measurement of the advanced nanocomposites reinforced concrete systems via both mathematical modeling and machine learning algorithm

Minggui Zhou[1], Gongxing Yan*[1,2], Danping Hu[1,2] and Haitham A. Mahmoud[3]

[1]*School of Intelligent Construction, Luzhou vocational and technical college, Luzhou 646000, Sichuan, China*
[2]*Luzhou Key Laboratory of Intelligent Construction and Low-carbon Technology, Luzhou 646000, China*
[3]*Industrial Engineering Department, College of Engineering, King Saud University, Riyadh 11421, Saudi Arabia*

(*Received October 6, 2020, Revised April 26, 2024, Accepted June 18, 2024*)

Abstract. This study investigates the thermal post-buckling behavior of concrete eccentric annular sector plates reinforced with graphene oxide powders (GOPs). Employing the minimum total potential energy principle, the plates' stability and response under thermal loads are analyzed. The Haber-Schaim foundation model is utilized to account for the support conditions, while the transform differential quadrature method (TDQM) is applied to solve the governing differential equations efficiently. The integration of GOPs significantly enhances the mechanical properties and stability of the plates, making them suitable for advanced engineering applications. Numerical results demonstrate the critical thermal loads and post-buckling paths, providing valuable insights into the design and optimization of such reinforced structures. This study presents a machine learning algorithm designed to predict complex engineering phenomena using datasets derived from presented mathematical modeling. By leveraging advanced data analytics and machine learning techniques, the algorithm effectively captures and learns intricate patterns from the mathematical models, providing accurate and efficient predictions. The methodology involves generating comprehensive datasets from mathematical simulations, which are then used to train the machine learning model. The trained model is capable of predicting various engineering outcomes, such as stress, strain, and thermal responses, with high precision. This approach significantly reduces the computational time and resources required for traditional simulations, enabling rapid and reliable analysis. This comprehensive approach offers a robust framework for predicting the thermal post-buckling behavior of reinforced concrete plates, contributing to the development of resilient and efficient structural components in civil engineering.

Keywords: advanced nanocomposites; concrete eccentric systems; machine learning algorithm; TDQM; thermal post buckling

1. Introduction

Simulating complex systems is of paramount importance for engineers across various disciplines) Kong *et al.* 2021, He *et al.* 2023). By leveraging advanced simulation techniques, engineers can analyze and predict the behavior of systems under a multitude of conditions without the need for physical prototypes, thus saving time and resources (He *et al.* 2024a, Luo *et al.* 2024). Simulations enable the visualization of complex phenomena, which would be difficult or impossible to observe directly (He *et al.* 2024b, c). This is crucial for understanding intricate interactions within a system and for identifying potential issues early in the design process (Wei *et al.* 2023, Wu *et al.* 2024). Through simulation, engineers can conduct extensive testing under different scenarios, including extreme conditions that would be dangerous or impractical to replicate in real life (Huang *et al.* 2021, Sun *et al.* 2023). This helps in ensuring the safety and reliability of the system. Moreover, simulations provide detailed insights into the system's performance, allowing engineers to optimize design parameters for enhanced efficiency and effectiveness (Huang *et al.* 2020, 2022). This is particularly important in fields such as aerospace, automotive, and civil engineering, where the performance and safety of structures and vehicles are critical (Huang *et al.* 2021, 2022). Simulating complex systems also aids in the development of innovative solutions (Liu *et al.* 2020, Yao *et al.* 2023). Engineers can experiment with new materials, configurations, and technologies in a virtual environment, leading to breakthroughs that might not be achievable through traditional methods (Yang *et al.* 2022, 2023). Additionally, simulations support iterative design processes, enabling rapid prototyping and refinement (Chen *et al.* 2023, Yang *et al.* 2023). Engineers can quickly test and modify designs based on simulation results, accelerating the development cycle (Li *et al.* 2023, Song *et al.* 2024). In terms of cost, simulations significantly reduce expenses associated with physical testing and prototyping (Lu *et al.* 2019, Li *et al.* 2023). By identifying potential flaws and optimizing designs virtually, companies can avoid costly rework and material wastage (Lu *et al.* 2017). This not only enhances economic efficiency but also contributes to sustainable engineering practices by minimizing resource consumption (Tian *et al.* 2021, Pang *et al.* 2022). Simulations are also valuable for educational purposes (Hu *et al.* 2023, Wu *et al.* 2023). They provide a hands-on learning experience for engineering students, allowing them to explore and understand complex systems in a controlled environment

---

*Corresponding author, Ph.D.,
E-mail: yaaangx@126.com

ISSN: 2287-237X (Print), 2287-2388 (Online)

(Han *et al*. 2023a, b). This practical exposure is essential for developing the skills required to tackle real-world engineering challenges (Liu *et al*. 2021, Taheri *et al*. 2021). Furthermore, the ability to simulate complex systems enhances collaborative efforts among engineering teams (Taheri *et al*. 2020, Feng *et al*. 2021). Simulations can be shared and analyzed collectively, fostering better communication and coordination (Firouzianhaji *et al*. 2021, Mehrabi *et al*. 2021). This is especially beneficial in large-scale projects involving multidisciplinary teams, where integrated solutions are necessary (Taheri *et al*. 2019, Mehrabi *et al*. 2021). In the context of predictive maintenance, simulations play a critical role (Xia *et al*. 2017, Toghroli *et al*. 2020). By modeling the degradation and failure modes of systems, engineers can anticipate maintenance needs and prevent unexpected downtimes (Horne *et al*. 2020). This proactive approach ensures the continuous and efficient operation of critical infrastructure and machinery (Mock *et al*. 2021). Overall, the importance of simulating complex systems for engineers cannot be overstated (Mock *et al*. 2024). It enables comprehensive analysis, optimization, and innovation, ultimately leading to safer, more efficient, and more reliable engineering solutions. As technology advances, the capabilities of simulation tools continue to expand, offering even greater potential for future engineering endeavors. Machine learning, a crucial angle of manufactured insights, empowers frameworks to independently recognize designs from information without requiring express programming, finding applications over different spaces, counting measurements (Qiu 2019, Qiu and Wang 2024). This predictive capability helps in identifying potential issues early in the design process, saving time and resources. By using mathematical and computational models, engineers can simulate various conditions and scenarios, ensuring that designs are robust and efficient. Modeling also facilitates optimization, enabling engineers to refine their designs for better performance and cost-effectiveness. It supports innovation by allowing the exploration of new materials, configurations, and technologies in a virtual environment. Additionally, modeling aids in understanding complex interactions within a system, providing deeper insights into its functionality and performance (Tounsi *et al*. 2013, Salari 2016, Ebrahimi and Jafari 2017, Ehyaei and Daman 2017, Kumar 2018, Wu *et al*. 2018, Ebrahimi *et al*. 2019a, b, Ebrahimi and Salari 2019, Emdadi *et al*. 2019, Ghannadpour and Moradi 2019, Dehshahri *et al*. 2020, Zhu *et al*. 2020). Furthermore, modeling enhances safety by allowing engineers to assess the effects of extreme conditions and identify potential failure points. It also supports compliance with industry standards and regulations by providing a means to test and validate designs. Overall, modeling is an indispensable tool for mechanical engineers, driving efficiency, innovation, and safety in engineering practice.

According to the published articles in the literature, there is no research on the thermal post buckling measurement of the advanced nanocomposites reinforced concrete systems via both mathematical modeling and machine learning algorithm. This study investigates the thermal post-buckling behavior of concrete eccentric annular sector plates reinforced with GOPs. Employing the minimum total potential energy principle, the plates' stability and response under thermal loads are analyzed. The Haber-Schaim foundation model is utilized to account for the support conditions, while the transform differential quadrature method is applied to solve the governing differential equations efficiently. The integration of GOPs significantly enhances the mechanical properties and stability of the plates, making them suitable for advanced engineering applications. Numerical results demonstrate the critical thermal loads and post-buckling paths, providing valuable insights into the design and optimization of such reinforced structures. This study presents a machine learning algorithm designed to predict complex engineering phenomena using datasets derived from presented mathematical modeling. By leveraging advanced data analytics and machine learning techniques, the algorithm effectively captures and learns intricate patterns from the mathematical models, providing accurate and efficient predictions. The methodology involves generating comprehensive datasets from mathematical simulations, which are then used to train the machine learning model. The trained model is capable of predicting various engineering outcomes, such as stress, strain, and thermal responses, with high precision. This approach significantly reduces the computational time and resources required fortraditional simulations, enabling rapid and reliable analysis. The results show that some geometrical and physical parameters has important role in the thermal post buckling measurement of the advanced nanocomposites reinforced concrete systems.

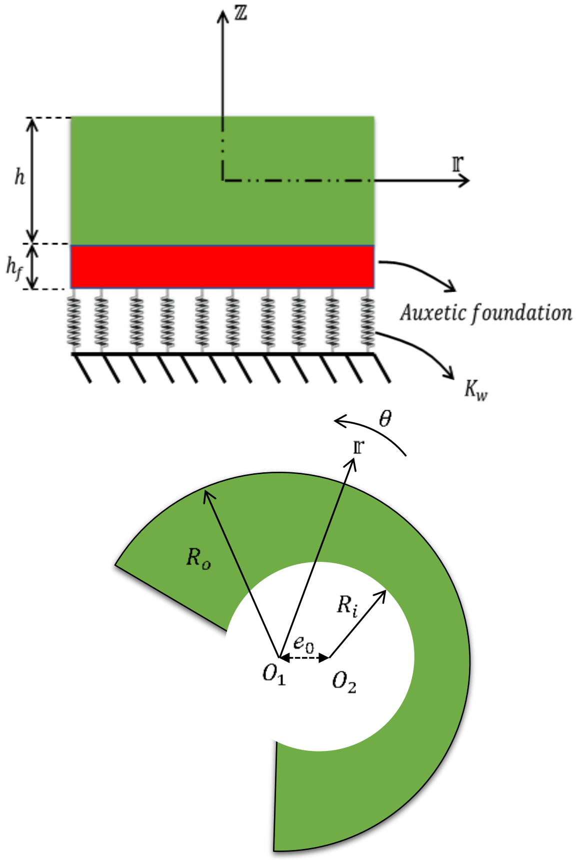

Fig. 1 An eccentric annular section plate diagram

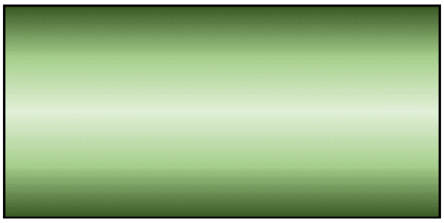

(a) Pattern 1 of GOP

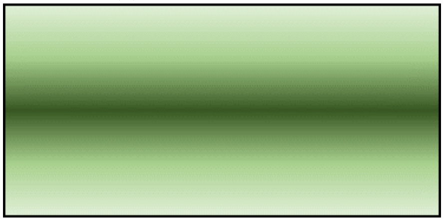

(b) Pattern 2 of GOP

(c) Pattern 3 of GOP

Fig. 2 The various distribution of GOP reinforcement

Table 1 Material properties of the system (Zhang *et al.* 2020)

Concrete (matrix)	GOPs
$v_m = 0.2$	$v_{GOP} = 0.165$
$\rho_m \,(\frac{kg}{m^3}) = 2300$	$\rho_{GOP} \,(\frac{kg}{m^3}) = 1090$
$E_m \,(Gpa) = 25$	$E_{GOP} \,(Gpa) = 444.8$
	$d_{GOP}(nm) = 500$
	$t_{GOP}(nm) = 0.95$

2. Basic equation

Examine the peculiar system shown in Fig. 1 that is positioned on an auxetic concrete base. Fig. 1 provides specifics on the construction's geometry and other pertinent aspects.

2.1 Graphene origami-enabled auxetic metamaterial

The various distribution of GOP reinforcement is given in Fig. 2.

The material properties of the GOPs reinforcement and concrete matrix are listed in Table 1.

2.2 Effective material properties for nanocomposites

The material properties are ascertained by extending the Halpin-Tsai homogenization technique. Currently, the Young's modulus may be written as (Zhang *et al.* 2020):

$$E_c = 0.49 \times \frac{1 + \xi_L \eta_L V_{GOP}}{1 - \eta_L V_{GOP}} \times E_m \tag{1}$$

$$+0.51 \times \frac{1 + \xi_t \eta_t V_{GOP}}{1 - \eta_t V_{GOP}} \times E_m$$

in which, $\xi_L = \xi_t = 2\frac{d_{GOP}}{h_{GOP}}$, $V_{GOP}^* = \frac{W_{GOP}}{W_{GOP} + \left(\frac{\rho_{GPL}}{\rho_M}\right)(1 - W_{GOP})}$, $\eta_l = -\frac{1-\left(\frac{E_{GOP}}{E_M}\right)}{\xi_l + \left(\frac{E_{GOP}}{E_m}\right)}$, and $\eta_t = -\frac{1-\left(\frac{E_{GOP}}{E_M}\right)}{\xi_t + \left(\frac{E_{GOP}}{E_m}\right)}$. The effective Poisson's ratio may be obtained by using the mixing rule from

$$v_c = \nu_{GOP} V_{GOP} + \nu_m (1 - V_{GOP}) \tag{2}$$

Furthermore, effective shear modulus is required.

$$G_c = \frac{E_c}{2(1 + v_c)} \tag{3}$$

Finally, the direction of thickness may be supplied together with the subsequent GOP distribution kinds:

$$X - GOP: V_{GOP}(k) = 4V_{GOP}^* \left|\frac{\mathbb{z}_k}{h}\right|, \tag{4a}$$

$$O - GOP: V_{GOP}(k) = 2V_{GOP}^* \left(1 - 2\left|\frac{\mathbb{z}_k}{h}\right|\right), \tag{4b}$$

$$UD - GOP: V_{GOP}(k) = V_{GOP}^*. \tag{4c}$$

Here, $\mathbb{z}_k = -\frac{h}{2} + \frac{(k-1)\times h}{N_L - 1}$, and $k = 1,2,3,\ldots,N_L$. It is now your job to use the following form Ref to compute the GOPR nanocomposite's coefficient of thermal expansion (CTE) (Guida-Pietrasanta *et al.* 2005)

$$\alpha_c = \alpha_M + \frac{\alpha_M + \alpha_{GOP}}{\frac{1}{K_M} + \frac{1}{K_{GOP}}} \left[\frac{1}{K_{eff}} + \frac{1}{K_M}\right] \tag{5}$$

2.3 Displacement field

The displacement fields of the present system may be approximated using the following formulation in accordance with the first order shear deformation theory:

$$\begin{aligned} \mathfrak{A}_{\mathbb{r}}(\mathbb{r}, \theta, \mathbb{z}) &= \mathfrak{A}_{\mathbb{r}0}(\mathbb{r}, \theta) + \mathbb{z}\mathfrak{A}_{\mathbb{r}1}(\mathbb{r}, \theta), \\ \mathfrak{A}_{\theta}(\mathbb{r}, \theta, \mathbb{z}) &= \mathfrak{A}_{\theta 0}(\mathbb{r}, \theta) + \mathbb{z}\mathfrak{A}_{\theta 1}(\mathbb{r}, \theta), \\ \mathfrak{A}_{\mathbb{z}}(\mathbb{r}, \theta, \mathbb{z}) &= \mathfrak{A}_{\mathbb{z}0}(\mathbb{r}, \theta). \end{aligned} \tag{6}$$

Furthermore, strain displacement has the following definition (Sadd 2009)

$$\begin{gathered} \mathcal{E}_{\mathbb{r}\mathbb{r}} = \frac{\partial \mathfrak{A}_{\mathbb{r}}}{\partial \mathbb{r}} + \frac{1}{2}\left(\frac{\partial \mathfrak{A}_{\mathbb{z}0}}{\partial \mathbb{r}}\right)^2, \mathcal{E}_{\theta\theta} = \frac{1}{\mathbb{r}}\left(\mathfrak{A}_{\mathbb{r}} + \frac{\partial \mathfrak{A}_{\theta}}{\partial \theta}\right) + \\ \frac{1}{2\mathbb{r}^2}\left(\frac{\partial \mathfrak{A}_{\mathbb{z}0}}{\partial \theta}\right)^2, \mathcal{E}_{\mathbb{r}\mathbb{z}} = \frac{\partial \mathfrak{A}_{\mathbb{r}}}{\partial \mathbb{z}} + \frac{\partial \mathfrak{A}_{\mathbb{z}}}{\partial \mathbb{r}}, \\ \mathcal{E}_{\mathbb{r}\theta} = \frac{1}{\mathbb{r}}\frac{\partial \mathfrak{A}_{\mathbb{r}}}{\partial \theta} + \frac{\partial \mathfrak{A}_{\theta}}{\partial \mathbb{r}} - \frac{\mathfrak{A}_{\theta}}{\mathbb{r}} + \frac{1}{\mathbb{r}}\frac{\partial \mathfrak{A}_{\mathbb{z}0}}{\partial \theta}\frac{\partial \mathfrak{A}_{\mathbb{z}0}}{\partial \mathbb{r}}, \\ \mathcal{E}_{\theta\mathbb{z}} = \frac{\partial \mathfrak{A}_{\theta}}{\partial \mathbb{z}} + \frac{1}{\mathbb{r}}\frac{\partial \mathfrak{A}_{\mathbb{z}}}{\partial \theta}. \end{gathered} \tag{7}$$

Next, the components of non-null strain are specified.

$$\{\mathcal{E}\} = \{\mathcal{E}^0\} + \mathbb{z}\{\mathcal{E}^1\}, \tag{8a}$$

$$\{\mathcal{E}\} = \begin{Bmatrix} \mathcal{E}_{\mathbb{r}\mathbb{r}} \\ \mathcal{E}_{\theta\theta} \\ \mathcal{E}_{\theta\mathbb{z}} \\ \mathcal{E}_{\mathbb{r}\mathbb{z}} \\ \mathcal{E}_{\mathbb{r}\theta} \end{Bmatrix}, \tag{8b}$$

$$\{\mathcal{E}^0\}=\begin{Bmatrix}\frac{\partial\mathfrak{U}_{\mathbb{r}0}}{\partial\mathbb{r}}+\frac{1}{2}(\frac{\partial\mathfrak{U}_{\mathbb{z}0}}{\partial\mathbb{r}})^2\\ \frac{1}{\mathbb{r}}(\frac{\partial\mathfrak{U}_{\theta0}}{\partial\theta}+\mathfrak{U}_{\mathbb{r}0})+\frac{1}{2\mathbb{r}^2}(\frac{\partial\mathfrak{U}_{\mathbb{z}0}}{\partial\theta})^2\\ \frac{1}{\mathbb{r}}\frac{\partial\mathfrak{U}_{\mathbb{z}0}}{\partial\theta}+\mathfrak{U}_{\theta1}\\ \frac{\partial\mathfrak{U}_{\mathbb{z}0}}{\partial\mathbb{r}}+\mathfrak{U}_{\mathbb{r}1}\\ \frac{\partial\mathfrak{U}_{\theta0}}{\partial\mathbb{r}}+\frac{1}{\mathbb{r}}(\frac{\partial\mathfrak{U}_{\mathbb{r}0}}{\partial\theta}-\mathfrak{U}_{\theta0})+\frac{1}{\mathbb{r}}\frac{\partial\mathfrak{U}_{\mathbb{z}0}}{\partial\theta}\frac{\partial\mathfrak{U}_{\mathbb{z}0}}{\partial\mathbb{r}}\end{Bmatrix},$$

$$\{\mathcal{E}^1\}=\begin{Bmatrix}\frac{\partial\mathfrak{U}_{\mathbb{r}1}}{\partial\mathbb{r}}\\ \frac{1}{\mathbb{r}}(\frac{\partial\mathfrak{U}_{\theta1}}{\partial\theta}+\mathfrak{U}_{\mathbb{r}1})\\ 0\\ 0\\ \frac{\partial\mathfrak{U}_{\theta1}}{\partial\mathbb{r}}+\frac{1}{\mathbb{r}}(\frac{\partial\mathfrak{U}_{\mathbb{r}1}}{\partial\theta}-\mathfrak{U}_{\theta1})\end{Bmatrix}.$$

The chosen thermomechanical coupled problem's constitutive relations are (He *et al*. 2021)

$$\begin{Bmatrix}\mathfrak{T}_{\mathbb{r}\mathbb{r}}\\ \mathfrak{T}_{\theta\theta}\\ \mathfrak{T}_{\theta\mathbb{z}}\\ \mathfrak{T}_{\mathbb{r}\mathbb{z}}\\ \mathfrak{T}_{\mathbb{r}\theta}\end{Bmatrix}=\begin{bmatrix}\frac{E_c}{1-v_c^2} & \frac{E_cv_c}{1-v_c^2} & 0 & 0 & 0\\ \frac{E_cv_c}{1-v_c^2} & \frac{E_c}{1-v_c^2} & 0 & 0 & 0\\ 0 & 0 & k_s\frac{E_c}{2(1+v_c)} & 0 & 0\\ 0 & 0 & 0 & k_s\frac{E_c}{2(1+v_c)} & 0\\ 0 & 0 & 0 & 0 & \frac{E_c}{2(1+v_c)}\end{bmatrix}\times\left(\begin{Bmatrix}\mathcal{E}_{\mathbb{r}\mathbb{r}}\\ \mathcal{E}_{\theta\theta}\\ \mathcal{E}_{\theta\mathbb{z}}\\ \mathcal{E}_{\mathbb{r}\mathbb{z}}\\ \mathcal{E}_{\mathbb{r}\theta}\end{Bmatrix}-\Delta T\begin{Bmatrix}\alpha_c\\ \alpha_c\\ 0\\ 0\\ 0\end{Bmatrix}\right) \quad (9)$$

The corrective shear factor of FSDT, denoted byk_s in the aforementioned equations, is set to $5/(6-v_c)$ for each structural layer (Efraim and Eisenberger 2007).

2.4 Minimum total potential energy

It is now possible to describe the minimal total potential energy concept as (Chen *et al*. 2017).

$$(\delta\mho_e-\delta\mho_w)=0 \quad (10)$$

The following descriptions clarify the quantities shown above.

$$\mho_e=\int\{\mathfrak{T}_{\mathbb{r}\mathbb{r}}\mathcal{E}_{\mathbb{r}\mathbb{r}}+\mathfrak{T}_{\theta\theta}\mathcal{E}_{\theta\theta}+\mathfrak{T}_{\theta\mathbb{z}}\mathcal{E}_{\theta\mathbb{z}}+\mathfrak{T}_{\mathbb{r}\mathbb{z}}\mathcal{E}_{\mathbb{r}\mathbb{z}}+\mathfrak{T}_{\mathbb{r}\theta}\mathcal{E}_{\mathbb{r}\theta}\}dV \quad (11)$$

The following is the mathematical depiction of an auxetic Haber-Schaim foundation in the Cartesian coordinate system (Behravan-Rad and Jafari 2020):

$$\delta\mho_w=\int_A\left(K_w\mathfrak{U}_{\mathbb{z}0}+D_f\nabla^4\mathfrak{U}_{\mathbb{z}0}\right)\delta\mathfrak{U}_{\mathbb{z}0}dA \quad (12)$$

The Poisson's ratio of the auxetic foundation, the thickness of the foundation plate, and the Winkler coefficient are indicated by v_f, h_f and K_w respectively, in Eq. (12). D_f also equals $\frac{E_f{h_f}^3}{12(1-v_f^2)}$. The following equations may be generated by conducting mathematical operations and inserting Eqs. (11) and (12) into Eq. (10).

$$\delta\mathfrak{U}_{\mathbb{r}0}:\frac{\partial\mathbb{N}_{\mathbb{r}\mathbb{r}}}{\partial\mathbb{r}}+\frac{1}{\mathbb{r}}\frac{\partial\mathbb{N}_{\mathbb{r}\theta}}{\partial\theta}+\frac{1}{\mathbb{r}}(\mathbb{N}_{\mathbb{r}\mathbb{r}}-\mathbb{N}_{\theta\theta})=0 \quad (13a)$$

$$\delta\mathfrak{U}_{\theta0}:\frac{1}{\mathbb{r}}\frac{\partial\mathbb{N}_{\theta\theta}}{\partial\theta}+\frac{\partial\mathbb{N}_{\mathbb{r}\theta}}{\partial\mathbb{r}}+\frac{2}{\mathbb{r}}\mathbb{N}_{\mathbb{r}\theta}=0 \quad (13b)$$

$$\begin{aligned}&\delta\mathfrak{U}_{\mathbb{z}0}:\frac{\partial\mathbb{Q}_{\mathbb{r}\mathbb{z}}}{\partial\mathbb{r}}+\frac{1}{\mathbb{r}}\frac{\partial\mathbb{Q}_{\theta\mathbb{z}}}{\partial\theta}+\frac{1}{\mathbb{r}}\mathbb{Q}_{\mathbb{r}\mathbb{z}}\\&+\frac{1}{\mathbb{r}}\frac{\partial}{\partial\mathbb{r}}\left(\mathbb{r}\mathbb{N}_{\mathbb{r}\mathbb{r}}\frac{\partial\mathfrak{U}_{\mathbb{z}0}}{\partial\mathbb{r}}+\mathbb{N}_{\mathbb{r}\theta}\frac{\partial\mathfrak{U}_{\mathbb{z}0}}{\partial\theta}\right)\\&+\frac{1}{\mathbb{r}}\frac{\partial}{\partial\theta}\left(\frac{1}{\mathbb{r}}\mathbb{N}_{\theta\theta}\frac{\partial\mathfrak{U}_{\mathbb{z}0}}{\partial\theta}+\mathbb{N}_{\mathbb{r}\theta}\frac{\partial\mathfrak{U}_{\mathbb{z}0}}{\partial\mathbb{r}}\right)\\&-\left(K_w\mathfrak{U}_{\mathbb{z}0}+D_f\nabla^4\mathfrak{U}_{\mathbb{z}0}\right)=0\end{aligned} \quad (13c)$$

$$\delta\mathfrak{U}_{\mathbb{r}1}:\frac{\partial\mathbb{M}_{\mathbb{r}\mathbb{r}}}{\partial\mathbb{r}}+\frac{1}{\mathbb{r}}\frac{\partial\mathbb{M}_{\mathbb{r}\theta}}{\partial\theta}+\frac{1}{\mathbb{r}}(\mathbb{M}_{\mathbb{r}\mathbb{r}}-\mathbb{M}_{\theta\theta})-\mathbb{Q}_{\mathbb{r}\mathbb{z}}=0 \quad (13d)$$

$$\delta\mathfrak{U}_{\theta1}:\frac{1}{\mathbb{r}}\frac{\partial\mathbb{M}_{\theta\theta}}{\partial\theta}+\frac{\partial\mathbb{M}_{\mathbb{r}\theta}}{\partial\mathbb{r}}+\frac{2}{\mathbb{r}}\mathbb{M}_{\mathbb{r}\theta}-\mathbb{Q}_{\theta\mathbb{z}}=0 \quad (13e)$$

In light of this, the boundary conditions are established.

$$\delta\mathfrak{U}_{\mathbb{r}0}=0 \quad \text{or} \quad (\mathbb{r}\mathbb{N}_{\mathbb{r}\mathbb{r}})\hat{n}_{\mathbb{r}}+(\mathbb{N}_{\mathbb{r}\theta})\hat{n}_\theta=0 \quad (14a)$$

$$\delta\mathfrak{U}_{\theta0}=0 \quad \text{or} \quad (\mathbb{r}\mathbb{N}_{\mathbb{r}\theta})\hat{n}_{\mathbb{r}}+(\mathbb{N}_{\theta\theta})\hat{n}_\theta=0 \quad (14b)$$

$$\begin{aligned}&\delta\mathfrak{U}_{\mathbb{z}0}=0 \ \text{ or } \left\{\mathbb{r}\mathbb{Q}_{\mathbb{r}\mathbb{z}}+\mathbb{r}\mathbb{N}_{\mathbb{r}\mathbb{r}}\frac{\partial\mathfrak{U}_{\mathbb{z}0}}{\partial\mathbb{r}}+\mathbb{N}_{\mathbb{r}\theta}\frac{\partial\mathfrak{U}_{\mathbb{z}0}}{\partial\theta}\right\}\hat{n}_{\mathbb{r}}\\&+\left\{\mathbb{Q}_{\theta\mathbb{z}}+\frac{\mathbb{N}_{\theta\theta}}{\mathbb{r}}\frac{\partial\mathfrak{U}_{\mathbb{z}0}}{\partial\theta}+\mathbb{N}_{\mathbb{r}\theta}\frac{\partial\mathfrak{U}_{\mathbb{z}0}}{\partial\mathbb{r}}\right\}\hat{n}_\theta=0\end{aligned} \quad (14c)$$

$$\delta\mathfrak{U}_{\mathbb{r}1}=0 \quad \text{or} \quad (\mathbb{r}\mathbb{M}_{\mathbb{r}\mathbb{r}})\hat{n}_{\mathbb{r}}+(\mathbb{M}_{\mathbb{r}\theta})\hat{n}_\theta=0 \quad (14d)$$

$$\delta\mathfrak{U}_{\theta0}=0 \quad \text{or} \quad (\mathbb{r}\mathbb{M}_{\mathbb{r}\theta})\hat{n}_{\mathbb{r}}+(\mathbb{M}_{\theta\theta})\hat{n}_\theta=0 \quad (14e)$$

The following equation may be used to determine the stress resultants according to the first-order shear deformation theory, which comprise moments $\mathbb{M}_{ij}$, shear forces $\mathbb{Q}_{ij}$, and in-plane forces $\mathbb{N}_{ij}$.

$$(\mathbb{N}_{\mathbb{r}\mathbb{r}},\mathbb{N}_{\theta\theta},\mathbb{N}_{\mathbb{r}\theta})=\int_{-\frac{h}{2}}^{\frac{h}{2}}(\mathfrak{T}_{\mathbb{r}\mathbb{r}},\mathfrak{T}_{\theta\theta},\mathfrak{T}_{\mathbb{r}\theta})d\mathbb{z} \quad (15a)$$

$$(\mathbb{M}_{\mathbb{r}\mathbb{r}},\mathbb{M}_{\theta\theta},\mathbb{M}_{\mathbb{r}\theta})=\int_{-\frac{h}{2}}^{\frac{h}{2}}\mathbb{z}(\mathfrak{T}_{\mathbb{r}\mathbb{r}},\mathfrak{T}_{\theta\theta},\mathfrak{T}_{\mathbb{r}\theta})d\mathbb{z} \quad (15b)$$

$$(\mathbb{Q}_{\mathbb{r}\mathbb{z}},\mathbb{Q}_{\theta\mathbb{z}})=\int_{-\frac{h}{2}}^{\frac{h}{2}}(\mathfrak{T}_{\mathbb{r}\mathbb{z}},\mathfrak{T}_{\theta\mathbb{z}})d\mathbb{z} \quad (15c)$$

or

$$\begin{Bmatrix}\mathbb{N}_{\mathbb{r}\mathbb{r}}\\ \mathbb{N}_{\theta\theta}\\ \mathbb{N}_{\mathbb{r}\theta}\\ \mathbb{M}_{\mathbb{r}\mathbb{r}}\\ \mathbb{M}_{\theta\theta}\\ \mathbb{M}_{\mathbb{r}\theta}\\ \mathbb{Q}_{\mathbb{r}\mathbb{z}}\\ \mathbb{Q}_{\theta\mathbb{z}}\end{Bmatrix}=\begin{bmatrix}\mathfrak{a}_{11} & \mathfrak{a}_{12} & 0 & \mathfrak{b}_{11} & \mathfrak{b}_{12} & 0 & 0 & 0\\ \mathfrak{a}_{12} & \mathfrak{a}_{22} & 0 & \mathfrak{b}_{12} & \mathfrak{b}_{22} & 0 & 0 & 0\\ 0 & 0 & \mathfrak{a}_{66} & 0 & 0 & \mathfrak{b}_{66} & 0 & 0\\ \mathfrak{b}_{11} & \mathfrak{b}_{12} & 0 & \mathfrak{d}_{11} & \mathfrak{d}_{12} & 0 & 0 & 0\\ \mathfrak{b}_{12} & \mathfrak{b}_{22} & 0 & \mathfrak{d}_{12} & \mathfrak{d}_{22} & 0 & 0 & 0\\ 0 & 0 & \mathfrak{b}_{66} & 0 & 0 & \mathfrak{d}_{66} & 0 & 0\\ 0 & 0 & 0 & 0 & 0 & 0 & \mathfrak{a}_{55} & 0\\ 0 & 0 & 0 & 0 & 0 & 0 & 0 & \mathfrak{a}_{44}\end{bmatrix}\begin{Bmatrix}\mathcal{E}_{\mathbb{r}\mathbb{r}}^0\\ \mathcal{E}_{\theta\theta}^0\\ \mathcal{E}_{\mathbb{r}\theta}^0\\ \mathcal{E}_{\mathbb{r}\mathbb{r}}^1\\ \mathcal{E}_{\theta\theta}^1\\ \mathcal{E}_{\mathbb{r}\theta}^1\\ \mathcal{E}_{\mathbb{r}\mathbb{z}}^0\\ \mathcal{E}_{\theta\mathbb{z}}^0\end{Bmatrix} \quad (16)$$

$$-\begin{Bmatrix} \mathbb{N}^T \\ \mathbb{N}^T \\ 0 \\ \mathbb{M}^T \\ \mathbb{M}^T \\ 0 \\ 0 \\ 0 \end{Bmatrix}$$

in which the following formulas may be used to get the stretching ($\mathfrak{a}_{ij}$), stretching-bending ($\mathfrak{b}_{ij}$), bending coefficients ($\mathfrak{d}_{ij}$), thermally induced force ($\mathbb{N}^T$), and moment ($\mathbb{M}^T$):

$$\mathfrak{a}_{11} = \mathfrak{a}_{22} = \int_{-\frac{h}{2}}^{\frac{h}{2}} \frac{E_c}{1-v_c^2} d\mathbb{z}, \quad \mathfrak{a}_{12} = \int_{-\frac{h}{2}}^{\frac{h}{2}} \frac{E_c v_c}{1-v_c^2} d\mathbb{z} \tag{17a}$$

$$\mathfrak{a}_{55} = \mathfrak{a}_{44} = \int_{-\frac{h}{2}}^{\frac{h}{2}} k_s \frac{E_c}{2(1+v_c)} d\mathbb{z}, \quad \mathfrak{a}_{66} = \int_{-\frac{h}{2}}^{\frac{h}{2}} \frac{E_c}{2(1+v_c)} d\mathbb{z} \tag{17b}$$

$$\mathfrak{b}_{11} = \mathfrak{b}_{22} = \int_{-\frac{h}{2}}^{\frac{h}{2}} \frac{E_c}{1-v_c^2} \mathbb{z} d\mathbb{z}, \quad \mathfrak{b}_{12} = \int_{-\frac{h}{2}}^{\frac{h}{2}} \frac{E_c v_c}{1-v_c^2} \mathbb{z} d\mathbb{z} \tag{17c}$$

$$\mathfrak{b}_{66} = \int_{-\frac{h}{2}}^{\frac{h}{2}} \frac{E_c}{2(1+v_c)} \mathbb{z} d\mathbb{z}, \quad \mathfrak{d}_{11} = \mathfrak{d}_{22} = \int_{-\frac{h}{2}}^{\frac{h}{2}} \frac{E_c}{1-v_c^2} \mathbb{z}^2 d\mathbb{z} \tag{17d}$$

$$\mathfrak{d}_{12} = \int_{-\frac{h}{2}}^{\frac{h}{2}} \frac{E_c v_c}{1-v_c^2} \mathbb{z}^2 d\mathbb{z}, \quad \mathfrak{d}_{66} = \int_{-\frac{h}{2}}^{\frac{h}{2}} \frac{E_c}{2(1+v_c)} \mathbb{z}^2 d\mathbb{z} \tag{17e}$$

$$\mathbb{N}^T = \int_{-\frac{h}{2}}^{\frac{h}{2}} \frac{E_c \alpha_c}{1-v_c} \Delta T d\mathbb{z}, \quad \mathbb{M}^T = \int_{-\frac{h}{2}}^{\frac{h}{2}} \frac{E_c \alpha_c}{1-v_c} \mathbb{z} \Delta T d\mathbb{z} \tag{17f}$$

3. Solution procedure

3.1 The TDQ discretization algorithm

According to the transformed differential quadrature method (TDQM) the nonlinear equations are solved. Aspects of a sandwich eccentric annular plate in the domain of computation and physics is shown in Fig. 3.

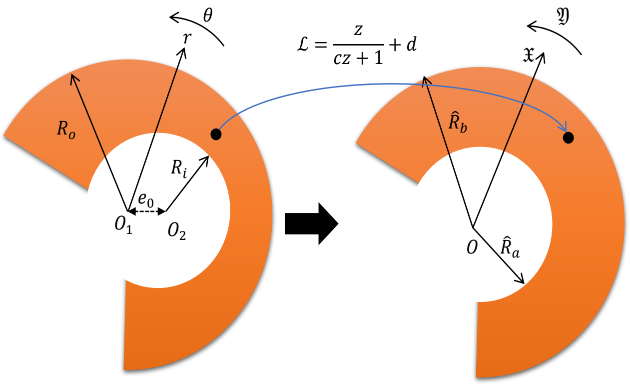

a) Physical domain b) Computational doma

Fig. 3 Aspects of a sandwich eccentric annular plate: computation and physics

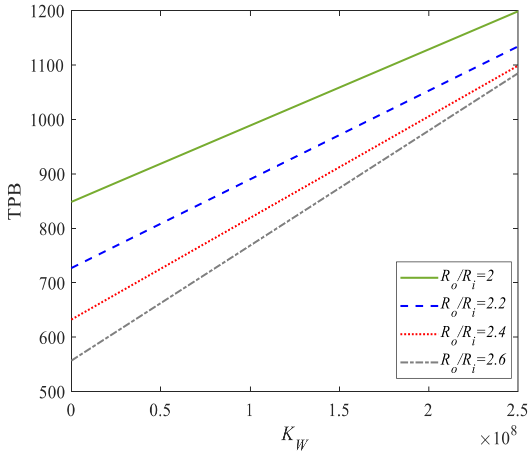

Fig. 4 The influences of radius ratio and Winkler coefficient parameter (K_W) on the TPB of the current annular plate structure

The bilinear conformal mapping approach, which is described below, is used to mathematically transform the eccentric annular plates (Fig. 4) to a shape without eccentricity in order to acquire the modified weighting factors for the plates (Chen *et al.* 2009).

$$\mathfrak{L} = \frac{\mathbb{z}}{\mathfrak{C}\mathbb{z}+1} + \mathbb{d} \tag{18}$$

In which

$$\mathfrak{C} = \frac{e_0}{\sqrt{e_0^4 - 2e_0^2(R_o^2 + R_i^2) + (R_i^2 - R_o^2)^2}}, \quad \mathbb{d} = \frac{\mathfrak{C}\hat{R}_i^2}{1 - (\mathfrak{C}\hat{R}_i)^2} \tag{19}$$

The outer radius of this domain ($\hat{R}_o$) and the in-plane geometrical properties of the eccentric annular plates are related to the inner radius of the altered domain, denoted as $\hat{R}_i$.

$$\hat{R}_i = \frac{\sqrt{4\mathfrak{C}^2 R_o^2 + 1} - 1}{2\mathfrak{C}^2 R_o}, \quad \hat{R}_o = \frac{\sqrt{4\mathfrak{C}^2 R_i^2 + 1 - 1}}{2\mathfrak{C}^2 R_i} \tag{20}$$

Eq. (18) may be obtained by replacing $\mathfrak{L} = \mathbb{r} + \bar{\mathrm{j}}\theta$ (where $\bar{\mathrm{j}} = \sqrt{-1}$) and $\mathbb{z} = \mathfrak{g} + \bar{\mathrm{j}}\mathfrak{h}$, and making the real and imaginary parts of the equation equal to each other.

$$\begin{aligned}
\mathbb{r} &= \frac{\sqrt{[\mathfrak{C}\mathfrak{g}^2(\mathfrak{C}\mathbb{d}+1) + \mathfrak{g}(2\mathfrak{C}\mathbb{d}+1)cos\mathfrak{h} + \mathbb{d}]^2 + \mathfrak{g}^2 sin^2\mathfrak{h}}}{\mathfrak{C}^2\mathfrak{g}^2 + 2\mathfrak{C}\mathfrak{g}cos\mathfrak{h} + 1} \\
\theta &= tan^{-1}\left[\frac{\mathfrak{g}sin\mathfrak{h}}{\mathfrak{C}\mathfrak{g}^2(\mathfrak{C}\mathbb{d}+1) + \mathfrak{g}(2\mathfrak{C}\mathbb{d}+1)cos\mathfrak{h} + \mathbb{d}}\right]
\end{aligned} \tag{21}$$

To determine the transformational connections between the coordinates $(\mathbb{r}, \theta)$ and $(\mathfrak{g}, \mathfrak{h})$, we use the chain rule of differentiation.

$$\begin{Bmatrix} \dfrac{\partial \mathscr{m}}{\partial \mathbb{r}} \\ \dfrac{\partial \mathscr{m}}{\partial \theta} \end{Bmatrix} = \begin{bmatrix} \mathbb{T}_{11} & \mathbb{T}_{12} \\ \mathbb{T}_{21} & \mathbb{T}_{22} \end{bmatrix} \begin{Bmatrix} \dfrac{\partial \mathscr{m}}{\partial \mathfrak{g}} \\ \dfrac{\partial \mathscr{m}}{\partial \mathfrak{h}} \end{Bmatrix} \tag{22}$$

The following equation defines $\mathbb{T}_{ij}$ (for $i, j = 1,2$), where $\mathscr{m}$ is an arbitrary function.

$$\begin{bmatrix} \mathbb{T}_{11} & \mathbb{T}_{12} \\ \mathbb{T}_{21} & \mathbb{T}_{22} \end{bmatrix} = \begin{bmatrix} \dfrac{\partial \mathbb{r}}{\partial \mathfrak{g}} & \dfrac{\partial \theta}{\partial \mathfrak{g}} \\ \dfrac{\partial \mathbb{r}}{\partial \mathfrak{h}} & \dfrac{\partial \theta}{\partial \mathfrak{h}} \end{bmatrix} \tag{23}$$

where

$$\begin{aligned}
\frac{\partial \mathbb{r}}{\partial \mathfrak{g}} &= \frac{cos\mathfrak{h}[\mathfrak{C}\mathfrak{g}^2(\mathfrak{C}\mathbb{d}+1) + \mathbb{d}] + 2\mathfrak{C}\mathbb{d}\mathfrak{g} + \mathfrak{g}}{(\mathfrak{C}^2\mathfrak{g}^2 + 2\mathfrak{C}\mathfrak{g}cos\mathfrak{h} + 1)\sqrt{\begin{matrix}\begin{bmatrix} \mathfrak{C}\mathfrak{g}^2(\mathfrak{C}\mathbb{d}+1) \\ +\mathfrak{g}(2\mathfrak{C}\mathbb{d}+1)cos\mathfrak{h} + \mathbb{d} \end{bmatrix}^2 \\ +\mathfrak{g}^2 sin^2\mathfrak{h}\end{matrix}}} \\
\frac{\partial \theta}{\partial \mathfrak{g}} &= \frac{[\mathbb{d} - \mathfrak{C}\mathfrak{g}^2(\mathfrak{C}\mathbb{d}+1)]sin\mathfrak{h}}{(\mathfrak{C}^2\mathfrak{g}^2 + 2\mathfrak{C}\mathfrak{g}cos\mathfrak{h} + 1)\begin{bmatrix} 2\mathbb{d}\mathfrak{g}(\mathfrak{C}\mathbb{d}+1)cos\mathfrak{h} \\ +(\mathfrak{C}\mathbb{d}\mathfrak{g} + \mathfrak{g})^2 + \mathbb{d}^2 \end{bmatrix}} \\
\frac{\partial \mathbb{r}}{\partial \mathfrak{h}} &= \frac{\mathfrak{g}[\mathfrak{C}\mathfrak{g}^2(\mathfrak{C}\mathbb{d}+1) - \mathbb{d}]sin\mathfrak{h}}{(\mathfrak{C}^2\mathfrak{g}^2 + 2\mathfrak{C}\mathfrak{g}cos\mathfrak{h} + 1)\sqrt{\begin{matrix}\begin{bmatrix} \mathfrak{C}\mathfrak{g}^2(\mathfrak{C}\mathbb{d}+1) \\ +\mathfrak{g}(2\mathfrak{C}\mathbb{d}+1)cos\mathfrak{h} + \mathbb{d} \end{bmatrix}^2 \\ +\mathfrak{g}^2 sin^2\mathfrak{h}\end{matrix}}} \\
\frac{\partial \theta}{\partial \mathfrak{h}} &= \frac{\mathfrak{g}\{[\mathfrak{C}\mathfrak{g}^2(\mathfrak{C}\mathbb{d}+1) + \mathbb{d}]cos\mathfrak{h} + 2\mathfrak{C}\mathbb{d}\mathfrak{g} + \mathfrak{g}\}}{(\mathfrak{C}^2\mathfrak{g}^2 + 2\mathfrak{C}\mathfrak{g}cos\mathfrak{h} + 1)\begin{bmatrix} 2\mathbb{d}\mathfrak{g}(\mathfrak{C}\mathbb{d}+1)cos\mathfrak{h} \\ +(\mathfrak{C}\mathbb{d}\mathfrak{g} + \mathfrak{g})^2 + \mathbb{d}^2 \end{bmatrix}}
\end{aligned} \tag{24}$$

According to the Gauss–Lobatto–Chebyshev grid point for $\mathbb{N}_{\mathfrak{g}}$ and $\mathbb{N}_{\mathfrak{h}}$ domain have:

$$\begin{aligned}
\mathfrak{g}_i &= \hat{R}_i + \frac{1}{2}\left\{1 - cos\left[\frac{(i-1)\pi}{\mathbb{N}_{\mathfrak{g}} - 1}\right]\right\}(\hat{R}_o - \hat{R}_i) \\
\mathfrak{h}_j &= \frac{\beta}{2}\left\{1 - cos\left[\frac{(j-1)\pi}{\mathbb{N}_{\mathfrak{h}} - 1}\right]\right\}
\end{aligned} \tag{25}$$

According to the DQM, discretization is possible for the first-order derivatives of the function $\mathscr{m} = (\mathfrak{A}_{\mathbb{r}0}, \mathfrak{A}_{\mathbb{r}1}, \mathfrak{A}_{\theta 0}, \mathfrak{A}_{\theta 1}, \mathfrak{A}_{\mathbb{z}0})$ at a given point $(\mathfrak{g}_i, \mathfrak{h}_j)$.

$$\begin{aligned}
\left(\frac{\partial \mathscr{m}}{\partial \mathfrak{g}}\right)_{(\mathfrak{g}_i, \mathfrak{h}_j)} &= \sum_{p=1}^{\mathbb{N}_{\mathfrak{g}}} \sum_{q=1}^{\mathbb{N}_{\mathfrak{h}}} \mathcal{A}_{ip}^{\mathfrak{g}} \delta_{jq} \mathscr{m}(\mathfrak{g}_p, \mathfrak{h}_q) \\
&= \sum_{p=1}^{\mathbb{N}_{\mathfrak{g}}} \sum_{q=1}^{\mathbb{N}_{\mathfrak{h}}} \mathcal{A}_{ip}^{\mathfrak{g}} \delta_{jq} \mathscr{m}_{pq} \\
\left(\frac{\partial \mathscr{m}}{\partial \mathfrak{h}}\right)_{(\mathfrak{g}_i, \mathfrak{h}_j)} & \textstyle\sum_{p=1}^{\mathbb{N}_{\mathfrak{g}}} \sum_{q=1}^{\mathbb{N}_{\mathfrak{h}}} \delta_{ip} \mathcal{A}_{jq}^{\mathfrak{g}} \mathscr{m}_{pq},
\end{aligned} \tag{26}$$

$$\text{for } i = 1, \ldots, \mathbb{N}_{\mathfrak{g}} \text{ and } j = 1, \ldots, \mathbb{N}_{\mathfrak{h}}$$

The first-order weighting coefficients associated with the γ-direction ($\gamma = \mathfrak{g}, \mathfrak{h}$) are denoted by $\mathcal{A}_{ij}^{\gamma}(\gamma = \mathfrak{g}, \mathfrak{h})$, and the Kronecker delta is denoted by δ_{ij}. Substitute Eq. (26) into Eq. (22) to get the first-order derivative of the field variable $\mathscr{m} = (\mathfrak{A}_{\mathbb{r}0}, \mathfrak{A}_{\mathbb{r}1}, \mathfrak{A}_{\theta 0}, \mathfrak{A}_{\theta 1}, \mathfrak{A}_{\mathbb{z}0})$ at a certain point $(\mathbb{r}_i, \theta_j)$ in the physical domain.

$$\begin{aligned}
\left(\frac{\partial \mathscr{m}}{\partial \mathbb{r}}\right)_{ij} &= \sum_{p=1}^{\mathbb{N}_{\mathbb{r}} = \mathbb{N}_{\mathfrak{g}}} \sum_{q=1}^{\mathbb{N}_{\theta} = \mathbb{N}_{\mathfrak{h}}} \begin{bmatrix} (\mathbb{T}_{11})_{ij} \mathcal{A}_{ip}^{\mathfrak{g}} \delta_{jq} \\ +(\mathbb{T}_{12})_{ij} \delta_{ip} \mathcal{A}_{jq}^{\mathfrak{h}} \end{bmatrix} \mathscr{m}_{pq} \\
\left(\frac{\partial \mathscr{m}}{\partial \theta}\right)_{ij} &= \sum_{p=1}^{\mathbb{N}_{\mathbb{r}} = \mathbb{N}_{\mathfrak{g}}} \sum_{q=1}^{\mathbb{N}_{\theta} = \mathbb{N}_{\mathfrak{h}}} \begin{bmatrix} (\mathbb{T}_{21})_{ij} \mathcal{A}_{ip}^{\mathfrak{g}} \delta_{jq} \\ +(\mathbb{T}_{22})_{ij} \delta_{ip} \mathcal{A}_{jq}^{\mathfrak{h}} \end{bmatrix} \mathscr{m}_{pq}
\end{aligned} \tag{27}$$

In which,

$$\begin{aligned}
\left(\frac{\partial \mathscr{m}}{\partial \mathbb{r}}\right)_{ij} &= \sum_{p=1}^{\mathbb{N}_{\mathbb{r}} = \mathbb{N}_{\mathfrak{g}}} \sum_{q=1}^{\mathbb{N}_{\theta} = \mathbb{N}_{\mathfrak{h}}} \tilde{\mathcal{A}}_{ijpq}^{\mathbb{r}} \mathscr{m}_{pq} \\
\left(\frac{\partial \mathscr{m}}{\partial \theta}\right)_{ij} &= \sum_{p=1}^{\mathbb{N}_{\mathbb{r}} = \mathbb{N}_{\mathfrak{g}}} \sum_{q=1}^{\mathbb{N}_{\theta} = \mathbb{N}_{\mathfrak{h}}} \tilde{\mathcal{A}}_{ijpq}^{\theta} \mathscr{m}_{pq}
\end{aligned} \tag{28}$$

$\tilde{\mathcal{A}}_{ipjq}^{\mathbb{r}}$ and $\tilde{\mathcal{A}}_{ipjq}^{\theta}$ can be defined as follows:

$$\begin{aligned}
\tilde{\mathcal{A}}_{ipjq}^{\mathbb{r}} &= (\mathbb{T}_{11})_{ij} \mathcal{A}_{ip}^{\mathfrak{g}} \delta_{jq} + (\mathbb{T}_{12})_{ij} \delta_{ip} \mathcal{A}_{jq}^{\mathfrak{h}} \\
\tilde{\mathcal{A}}_{ipjq}^{\theta} &= (\mathbb{T}_{21})_{ij} \mathcal{A}_{ip}^{\mathfrak{g}} \delta_{jq} + (\mathbb{T}_{22})_{ij} \delta_{ip} \mathcal{A}_{jq}^{\mathfrak{h}}
\end{aligned} \tag{29}$$

The similar method may be used to discretize the second-order derivatives at a point $(\mathbb{r}_i, \theta_j)$ in the physical domain of the field variable $\mathscr{m} = (\mathfrak{A}_{\mathbb{r}0}, \mathfrak{A}_{\mathbb{r}1}, \mathfrak{A}_{\theta 0}, \mathfrak{A}_{\theta 1}, \mathfrak{A}_{\mathbb{z}0}, \mathfrak{A}_{\mathbb{z}1})$.

$$\begin{aligned}
\left(\frac{\partial^2 \mathscr{m}}{\partial \mathbb{r}^2}\right)_{ij} &= \sum_{p=1}^{\mathbb{N}_{\mathbb{r}} = \mathbb{N}_{\rho}} \sum_{q=1}^{\mathbb{N}_{\theta} = \mathbb{N}_{\alpha}} \widetilde{\mathcal{B}}_{ijpq}^{\mathbb{r}} \mathscr{m}_{pq} \\
\left(\frac{\partial^2 \mathscr{m}}{\partial \theta^2}\right)_{ij} &= \sum_{p=1}^{\mathbb{N}_{\mathbb{r}} = \mathbb{N}_{\rho}} \sum_{q=1}^{\mathbb{N}_{\theta} = \mathbb{N}_{\alpha}} \widetilde{\mathcal{B}}_{ijpq}^{\theta} \mathscr{m}_{pq} \\
\left(\frac{\partial^2 \mathscr{m}}{\partial \mathbb{r} \partial \theta}\right)_{ij} &= \sum_{p=1}^{\mathbb{N}_{\mathbb{r}} = \mathbb{N}_{\rho}} \sum_{q=1}^{\mathbb{N}_{\theta} = \mathbb{N}_{\alpha}} \widetilde{\mathcal{B}}_{ijpq}^{\mathbb{r}\theta} \mathscr{m}_{pq}
\end{aligned} \tag{30}$$

The second-order derivatives' transformed weighting coefficients are shown in proportion to the first-order derivatives' weighting coefficients as follows:

$$\begin{aligned}
\widetilde{\mathcal{B}}_{ipjq}^{\mathbb{r}} &= \sum_{k=1}^{\mathbb{N}_{\mathbb{r}}} \sum_{l=1}^{\mathbb{N}_{\theta}} \tilde{\mathcal{A}}_{ikjl}^{\mathbb{r}} \tilde{\mathcal{A}}_{kplq}^{\mathbb{r}} \\
\widetilde{\mathcal{B}}_{ipjq}^{\mathbb{r}\theta} &= \sum_{k=1}^{\mathbb{N}_{\mathbb{r}}} \sum_{l=1}^{\mathbb{N}_{\theta}} \tilde{\mathcal{A}}_{ikjl}^{\mathbb{r}} \tilde{\mathcal{A}}_{kplq}^{\theta} \\
\widetilde{\mathcal{B}}_{ipjq}^{\theta} &= \sum_{k=1}^{\mathbb{N}_{\mathbb{r}}} \sum_{l=1}^{\mathbb{N}_{\theta}} \tilde{\mathcal{A}}_{ikjl}^{\theta} \tilde{\mathcal{A}}_{kplq}^{\theta}
\end{aligned} \tag{31}$$

Utilizing the above TDQM principles, solve Eqs. (13a–e) by replacing them with Eqs. (26)-(31) and (17a-f). As required, apply different boundary conditions using Eqs. (14a-e).

$$(\boldsymbol{\mathcal{K}}_{\mathrm{L}} - \Delta\mathbb{T}\boldsymbol{\mathcal{K}}_{\mathrm{T}} + \boldsymbol{\mathcal{K}}_{\mathrm{NL1}} + \boldsymbol{\mathcal{K}}_{\mathrm{NL2}})\mathbf{d} = 0 \tag{32}$$

Utilizing the iterative method outlined by Liew *et al.*, solve the nonlinear controlling Eq. (32) to determine the postbuckling equilibrium path (Liew *et al.* 2003).

4. Introduction to improved deep neural networks for measuring thermal post-buckling of advanced nanocomposites reinforced concrete systems

Advancements in materials science have introduced nanocomposites that enhance the performance of reinforced concrete systems. These advanced nanocomposites offer improved strength, durability, and thermal stability, making them ideal for modern construction applications. However, the thermal post-buckling behavior of these materials presents significant challenges due to their complex interactions under thermal loads. Accurately predicting this behavior is critical for the safety and reliability of structures that incorporate these advanced materials. Improved deep neural networks (DNNs) offer a sophisticated approach to tackle these challenges. By enhancing the architecture and learning capabilities of traditional neural networks, these improved models can better capture the intricate behaviors of nanocomposites reinforced concrete systems under thermal stresses. This introduction explores the role of improved DNNs in measuring and predicting the thermal post-buckling behavior of these advanced materials.

4.1 Understanding Thermal Post-Buckling

Thermal Post-Buckling refers to the structural deformation that occurs after a material has buckled due to thermal loads. This phenomenon is particularly complex in nanocomposites reinforced concrete systems, where the interaction between the nanocomposite materials and the concrete matrix under varying temperatures leads to nonlinear and heterogeneous responses.

4.1.1 Challenges in Measurement and Prediction

- Material Nonlinearity: Nanocomposites exhibit nonlinear mechanical behavior under thermal loads due to their composite nature.
- Geometric Nonlinearity: Post-buckling involves large deformations, making the problem inherently nonlinear.
- Heterogeneity: The distribution of nanomaterials within the concrete creates heterogeneous material properties.
- Temperature Variability: The properties of both nanocomposites and concrete change with temperature, adding complexity to the prediction models.

4.1.2 Role of Improved Deep Neural Networks

Improved Deep Neural Networks (DNNs) integrate advancements in neural network architectures and training methodologies to enhance their predictive capabilities. Key improvements include:

- Enhanced Architectures: Utilizing advanced network architectures such as Convolutional Neural Networks (CNNs), Recurrent Neural Networks (RNNs), and Transformer models to capture different aspects of the data.
- Feature Extraction: Improved methods for automatic feature extraction from complex datasets, crucial for understanding stress and strain distributions.
- Learning Algorithms: Advanced learning algorithms that enhance the network’s ability to model nonlinearity and heterogeneity.
- Optimization Techniques: Use of state-of-the-art optimization techniques to improve convergence and accuracy.

4.1.3 Advantages of Using Improved DNNs

- Higher Accuracy: Improved DNNs can model the complex interactions and nonlinearities more accurately than traditional methods.
- Robustness: These models are more robust to variations in data, enhancing the reliability of their predictions.
- Scalability: Capable of handling large datasets and complex simulations, making them suitable for extensive research and practical applications.
- Adaptability: Easily adaptable to new data and evolving understanding of material behaviors, leading to continuous improvement in predictions.

4.1.4 Applications

- Higher Accuracy

Improved DNNs can model the complex, nonlinear interactions between thermal loads and material responses more accurately than traditional methods. This is achieved through advanced architectures and learning algorithms that capture intricate patterns and dependencies in the data.

- Enhanced Robustness

The hybrid approach makes the model more robust to variations in data, improving the reliability of predictions. This robustness is critical in handling the heterogeneous nature of nanocomposites and the variable conditions they may encounter in real-world applications.

- Scalability

These models are capable of handling large datasets and complex simulations, making them suitable for extensive research and practical applications. They can be trained on diverse and voluminous data, enhancing their generalizability and applicability to different scenarios.

- Adaptability

Improved DNNs are easily adaptable to new data and evolving understanding of material behaviors. They can continuously improve their predictive capabilities by incorporating new information, ensuring they remain up-to-date with the latest research and developments.

- Automatic Feature Extraction

Improved methods for automatic feature extraction allow the network to identify and leverage relevant features from complex datasets without manual intervention. This is particularly useful for analyzing stress and strain distributions in nanocomposites reinforced concrete systems.

- Advanced Learning Algorithms

The use of state-of-the-art learning algorithms enhances the network’s ability to model nonlinearity and heterogeneity, which are inherent in the thermal post-buckling behavior of advanced nanocomposites. This leads to more accurate and reliable predictions.

- Optimization Techniques

Employing advanced optimization techniques improves the convergence and accuracy of the models. These techniques help in fine-tuning the network parameters, ensuring optimal performance and reducing the likelihood of overfitting or underfitting.

- Real-Time Monitoring and Prediction

Improved DNNs facilitate real-time monitoring and prediction of structural behavior under thermal loads. This capability is crucial for applications such as structural health monitoring, where timely detection of potential issues can prevent failures and enhance safety.

- Design Optimization

These models assist engineers in designing more resilient and efficient nanocomposite materials and structures. By accurately predicting thermal post-buckling behavior, improved DNNs enable optimization of material composition and structural design for better performance.

- Early Failure Detection

Improved DNNs provide early detection of potential failures, enabling preemptive maintenance and enhancing the safety of structures. This predictive capability helps in identifying issues before they escalate, allowing for timely interventions and reducing the risk of catastrophic failures.

- Integration with Modern Infrastructure

The adaptability and scalability of improved DNNs make them suitable for integration with modern infrastructure and smart systems. They can be part of an automated monitoring system that continuously assesses structural integrity and performance, ensuring long-term reliability and safety. In summary, improved deep neural networks offer significant advantages in measuring and predicting the thermal post-buckling behavior of advanced nanocomposites reinforced concrete systems. Their higher accuracy, robustness, scalability, and adaptability, along with advanced feature extraction and optimization techniques, make them a powerful tool in modern structural engineering and materials science. To provide a basic example of how you might implement an improved deep neural network (DNN) for predicting thermal post-buckling behavior in Python, I'll outline a simple code using TensorFlow and Keras. This example assumes you have a dataset of features (e.g., material properties, geometric parameters, and thermal load conditions) and corresponding labels (e.g., post-buckling responses). Here's how you can implement a simple DNN:

4.1.5 Step-by-Step Implementation

4.1.5.1 Install required libraries

```
pip install tensorflow pandas scikit-learn
```

4.1.5.2 Prepare the dataset

This step involves loading your dataset, preprocessing it, and splitting it into training and testing sets. For this example, let's assume you have a CSV file data.csv.

```
import pandas as pd
from sklearn.model_selection import train test_split
from sklearn.preprocessing import StandardScaler
#Load the dataset
data = pd.read_csv('data.csv')
# Assuming the last column is the label (post-buckling response)
X = data.iloc[:, :-1].values
y = data.iloc[:, -1].values
#Split the data into training and testing sets
X_train, X_test, y_train, y_test = train_test_split(X, y, test_size=0.2, random_state=42)
#Standardize the features
scaler StandardScaler()
X_train scaler.fit transform(X_train)
X_test = scaler.transform(X test)
```

4.1.5.3 Define the improved deep neural network

Here, we'll define a simple deep neural network using Keras.

```
import tensorflow as tf
from tensorflow.keras.models import Sequential
from tensorflow.keras.layers import Dense, Dropout
#Define the DNN model
def create model():
model = Sequential()
model.add(Dense(128, input_dim=X_train.shape[1], activation='relu'))
model.add(Dropout(0.2))
model.add(Dropout(0.2))
model.add(Dense(32, activation='relu'))
model.add(Dense(1, activation 'linear')) # For regression
model.compile(optimizer 'adam', loss
='mean_squared_error', metrics=['mae'])
return model
model = create_model()
```

4.1.5.4 Train the model

We'll train the model using the training dataset.

```
# Train the model history=model.fit(X_train, y_train, epochs=100, batch_size=32, validation_split=0.2)
```

Here's the complete code in one piece for clarity:

```
import pandas as pd
from sklearn.model selection import train test split
from sklearn.preprocessing import StandardScaler
import tensorflow as tf
from tensorflow.keras.models import Sequential
from tensorflow.keras.layers import Dense, Dropout
#Load the dataset
data = pd.read_csv('data.csv')
#Assuming the last column is the label (post-buckling response)
X= data.iloc[:, :-1].values
y = data.iloc[:, -1].values
#Split the data into training and testing sets
X_train, X_test, y_train, y_test = train_test_split(X, y, test_size=0.2, random_state=42)
#Standardize the features
scaler = StandardScaler()
X_train = scaler.fit_transform(X_train)
X_test = scaler.transform(X_test)
#Define the DNN model
def create_model():
model = Sequential()
model.add (Dense(128, input_dim=X_train.shape[1], activation = 'relu'))
```

Table 2 Comparing the results of sector plates' critical temperature rise (ΔT_{cr})

	CCCC	CSCS	SCSC	SSSS
Present	96.7456	93.0487	31.8866	29.3956
Ref. (Javani *et al.* 2020)	96.7456	93.0487	31.8866	29.3956

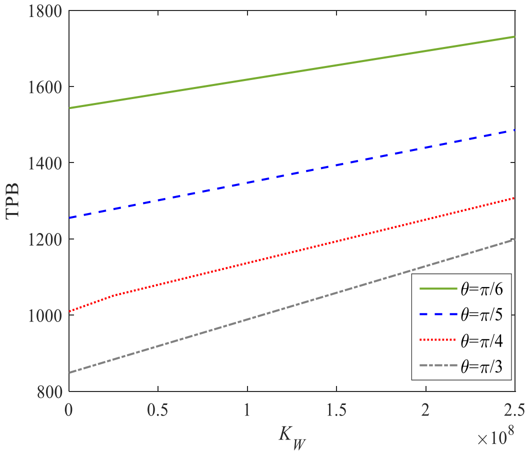

Fig. 5 The influences of sector annular plate's angle and Winkler coefficient parameter on the TPB of the current annular plate structure

```
model.add (Dropout(0.2))
model.add (Dropout(0.2))
model.add (Dense(1, activation='linear')) #For
regression
model.compile (optimizer 'adam', loss ='mean_squared_
error', metrics=['mae'])
```

5. Results and discussion

5.1 Validation

Table 1 presents a comparison of the current investigation's findings with those of previously published research in order to assess their validity. The objective of the comparative study is to examine and compare the sector plates structure's critical temperature increase with the findings from Ref. (Javani *et al.* 2020) for a range of boundary conditions. The current study's findings on the sector plates structure's critical temperature increase are in good agreement with those of Ref. (Javani *et al.* 2020). Additionally, using CCCC boundary conditions raises the critical temperature increase in comparison to other boundary condition types.

5.2 Parametric results

In this work, for the first time, the influences of various parameters on the thermal post buckling characteristics of the current annular plate structure surrounded by elastic-auxetic foundation is presented. To know about the influences of radius ratio and Winkler coefficient parameter (K_W) on the TPB of the current annular plate structure, Fig. 4 is presented. As is seen, an increase in the Kw due to increasing the stiffness in the structure results in increase in the TPB characteristics of the presented annular plate structure increases. Also, by increasing the radius ratio due to decreasing the stiffness of the system, the TPB characteristics of the presented annular plate structure decreases. This decrease in the higher values of K_W parameter is less than at the lower values of K_W parameter.

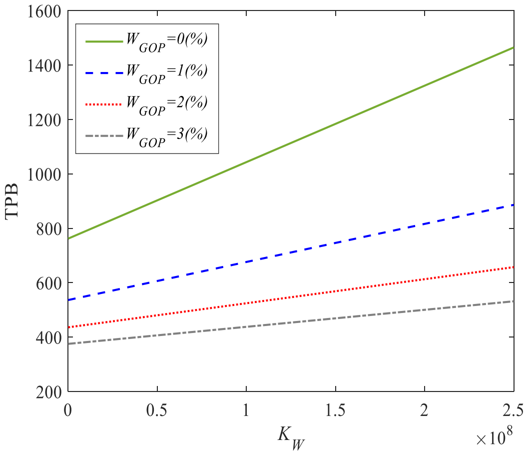

Fig. 6 The impacts of W_{GOP} and K_W on the TPB characteristics of the sector annular plate structure

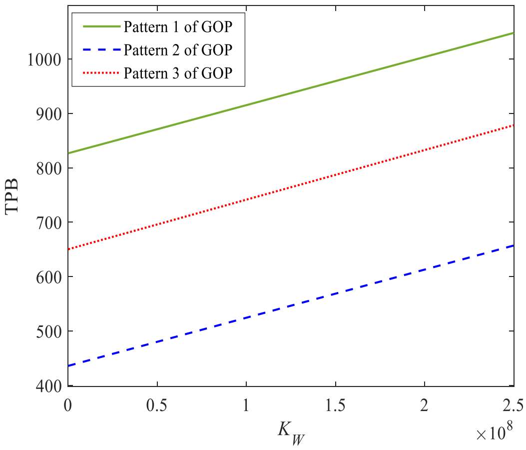

Fig. 7 The influences of GOP distribution pattern and K_W parameter on the TPB characteristics of the current sector annular plate structure

Fig. 5 shows the effects of the Winkler coefficient parameter and sector annular plate angle on the TPB of the present annular plate construction. As can be shown, the TPB characteristics of the annular plate structure are increased as the K_W rises as a consequence of the structure's increased stiffness. Moreover, the TPB characteristics of the proposed annular plate structure diminish as a result of a reduction in system stiffness, which raises the sector annular plate's angle.

The impacts of W_{GOP} and K_W on the TPB characteristics of the sector annular plate structure is presented in Fig. 6. As is mentioned, an increase in the W_{GOP} and K_W result in increase in the TPB characteristics of the presented sector annular plate structure. Also, the impact of GOP weight

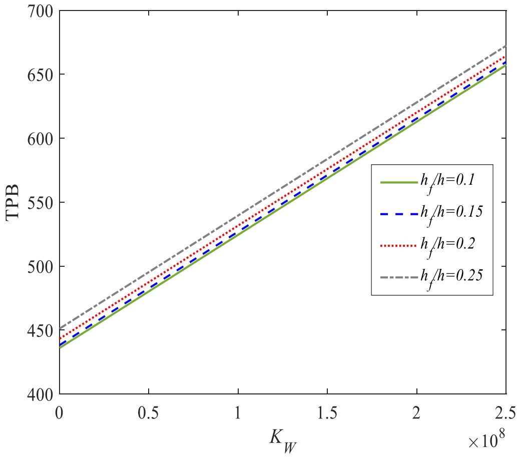

Fig. 8 The influences of auxetic foundation thickness ratio and K_W parameter on the TPB characteristics of the current sector annular plate structure

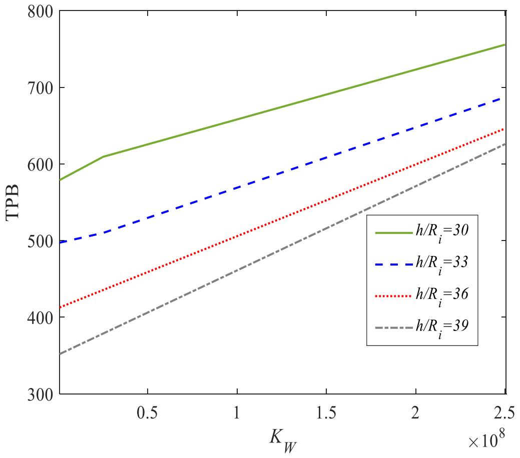

Fig. 9 The influences of thickness ratio (h/R_i) and Winkler coefficient parameter (K_W) on the TPB of the current annular plate structure

fraction on the TPB characteristics of the presented sector annular plate structure is more clear in the lower values of K_W parameter. Also, the impact of K_W on the TPB characteristics of the presented sector annular plate structure is more clear at the lower values of GOP weight fraction.

The influences of GOP distribution pattern and K_W parameter on the TPB characteristics of the current sector annular plate structure is shown in Fig. 7. As is seen, selecting pattern 1 of GOP has highest TPB than other patterns of GOP. Also, the impact of GOP distribution pattern on the TBP of the sector annular plate structure in all values of K_W is the same.

The influences of auxetic foundation thickness ratio and K_W parameter on the TPB characteristics of the current sector annular plate structure is shown in Fig. 8. As is seen, selecting higher values of auxetic foundation thickness ratio has highest TPB than other patterns of GOP. Also, the impact of auxetic foundation thickness ratio on the TBP of the sector annular plate structure in all values of K_W is the same.

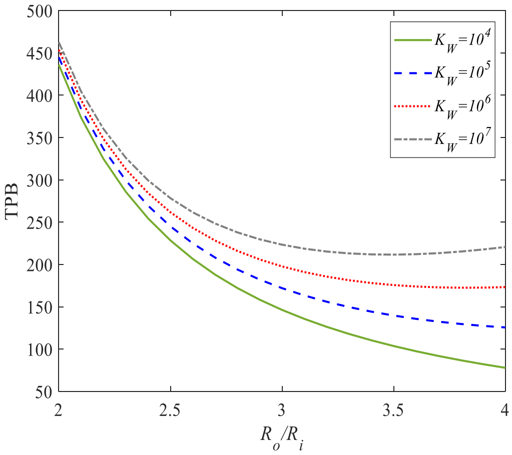

Fig. 10 The influences of radius ratio and Winkler coefficient on the TPB of the current sector annular plate structure

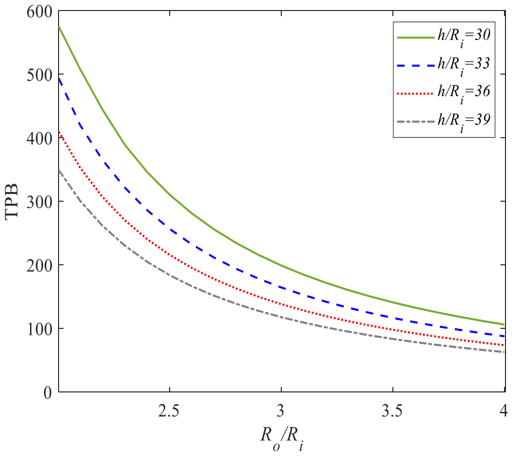

Fig. 11 The influences of radius ratio and h/R_i on the TPB of the current sector annular plate structure

To know about the influences of thickness ratio (h/R_i) and Winkler coefficient parameter (K_W) on the TPB of the current annular plate structure, Fig. 9 is presented. As is seen, an increase in the Kw due to increasing the stiffness in the structure results in increase in the TPB characteristics of the presented annular plate structure increases. Also, by increasing the h/R_i due to decreasing the stiffness of the system, the TPB characteristics of the presented annular plate structure decreases. This decrease in the higher values of K_W parameter is less than at the lower values of K_W parameter.

The influences of radius ratio and Winkler coefficient on the TPB of the current sector annular plate structure Fig. 10 is presented. As is seen, by increasing the R_0/R_i, the TPB decreases with different slopes. For more detail, at the lower values of R_0/R_i (less than 3), a huge decrease can be seen in the system while at the higher values (more than 3) the behavior of the system changes. Selecting higher values of K_W at the higher values of R_0/R_i, due to increasing the stability of the system due to increasing the K_W parameter, the TPB characteristics of the current structure increases. It can be concluded that, at the higher

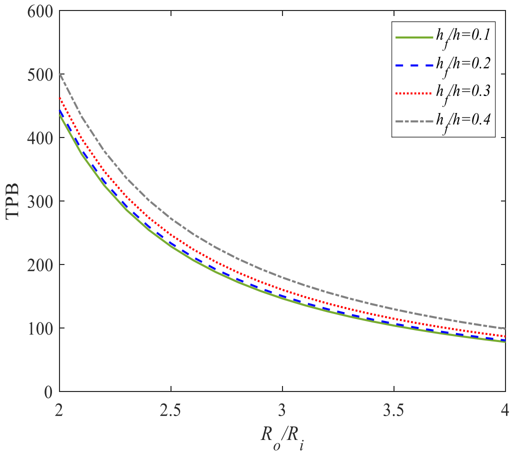

Fig. 12 The influences of radius ratio and h_f/h on the TPB of the current sector annular plate structure

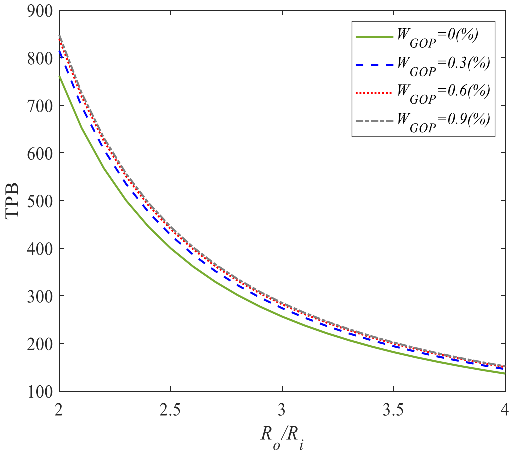

Fig. 13 The influences of radius ratio and W_{GOP} on the TPB of the current sector annular plate structure

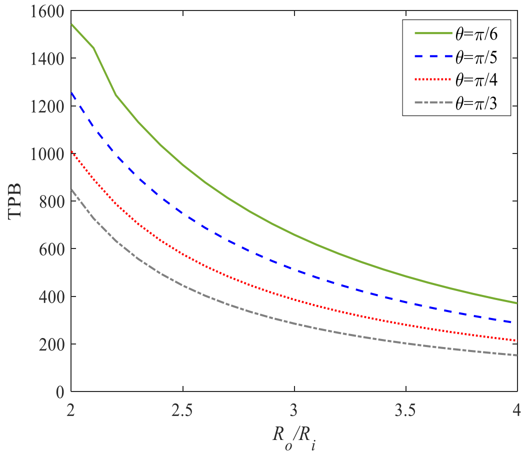

Fig. 14 The influences of radius ratio and θ on the TPB of the current sector annular plate structure

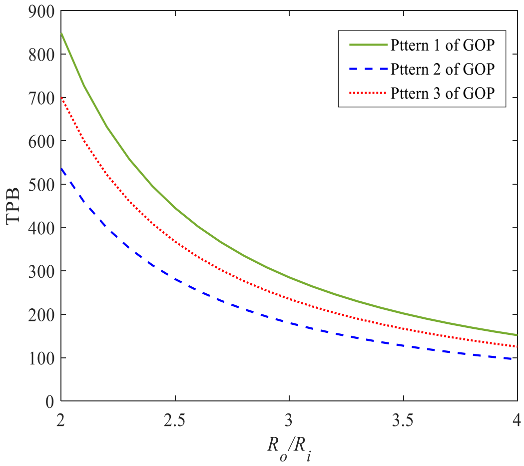

Fig. 15 The influences of radius ratio and GOP distribution pattern on the TPB of the current sector annular plate structure

values of R_0/R_i and K_W parameters, the stability of the system increases.

The influences of radius ratio and h/R_i on the TPB of the current sector annular plate structure Fig. 11 is presented. As is seen, by increasing the R_0/R_i, the TPB decreases with different slopes. For more detail, at the lower values of R_0/R_i (less than 3), a huge decrease can be seen in the system while at the higher values (more than 3) the behavior of the system changes. At the higher values of R_0/R_i the decreasing of the TPB due to increasing the R_0/R_i becomes slower than at the lower values of R_0/R_i. Also, by increasing the h/R_i the stability of the system and finally the TPB of the current sector annular plate structure decreases.

The influences of radius ratio and h_f/h on the TPB of the current sector annular plate structure Fig. 12 is presented. As is seen, by increasing the R_0/R_i, the TPB decreases with different slopes. For more detail, at the lower values of R_0/R_i (less than 3), a huge decrease can be seen in the system while at the higher values (more than 3) the behavior of the system changes. At the higher values of R_0/R_i the decreasing of the TPB due to increasing the R_0/R_i becomes slower than at the lower values of R_0/R_i. Also, by increasing the h_f/h the stability of the system and finally the TPB of the current sector annular plate structure increases.

The influences of radius ratio and W_{GOP} on the TPB of the current sector annular plate structure Fig. 13 is presented. As is seen, by increasing the R_0/R_i, the TPB decreases with different slopes. This issue has been explained in detail in the previous figures. By increasing the WGOP the stiffness of the structure and finally the TPB increases. This increase at the lower values of R_0/R_i is more clear than higher ones.

Fig. 14 presents the effects of radius ratio and θ on the TPB of the current sector annular plate construction. As can be seen, the TPB declines with varying slopes as the R_0/R_i increases. The preceding graphics provide a detailed explanation of this problem. The TPB and the structure's stiffness both drop when the sector annular plate structure's θ increases. It is easier to see this growth at smaller R_0/R_i numbers than at larger ones.

Fig. 15 presents the effects of GOP distribution pattern and radius ratio on the TPB of the current sector annular plate construction. As can be seen, the TPB declines with

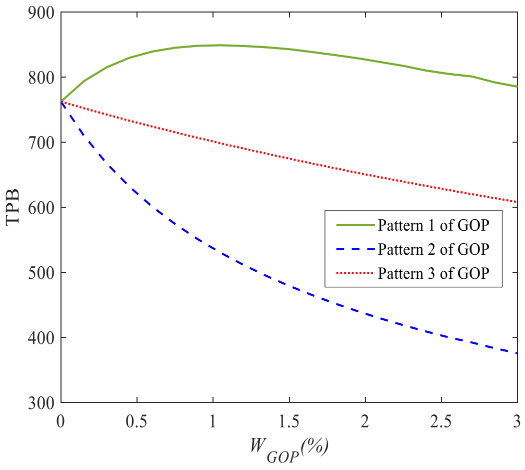

Fig. 16 The impacts of GOP distribution pattern and W_{GOP} on the TPB of the presented sector annular plate structure

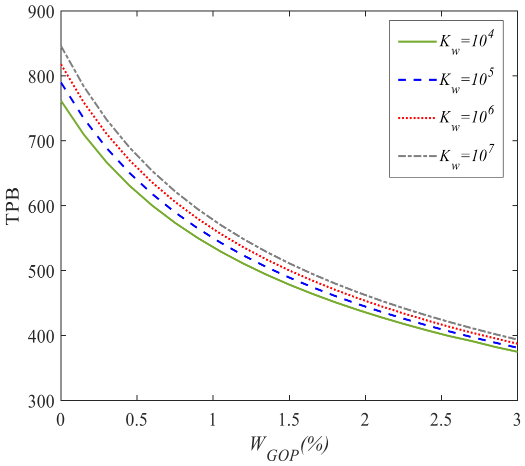

Fig. 17 The influences of W_{GOP} and K_W on the TPB of the current sector annular plate structure

varying slopes as the R_0/R_i increases. The preceding graphics provide a detailed explanation of this problem. The GOP distribution pattern's first pattern is chosen, which enhances the structure's stiffness and, ultimately, the TPB. It is easier to see this growth at smaller R_0/R_i numbers than at larger ones.

The impacts of GOP distribution pattern and W_{GOP} on the TPB of the presented sector annular plate structure is shown in Fig. 16. As is seen, GOP distribution pattern has great influence on the TPB characteristics of the presented structure. For more detail, considering pattern 1 of GOP, by increasing the W_{GOP} the TPB of the structure first increases and then decreases. This behavior for pattern 2 of GOP distribution pattern in inverse. Also, selecting pattern 3 of GOP results in a smooth decrease (with constant slope) in the TBP by increasing the W_{GOP}.

The influences of W_{GOP} and K_W on the TPB of the current sector annular plate structure Fig. 17 is presented. As is seen, by increasing the W_{GOP}, the TPB decreases with different slopes. This issue has been explained in detail in the previous figs. By increasing the K_W of the foundation the stiffness of the structure and finally the TPB increases.

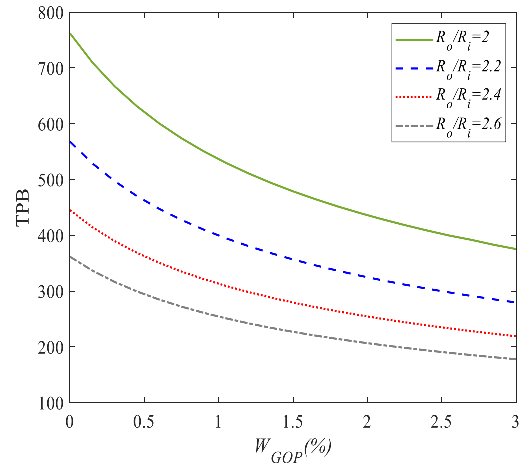

Fig. 18 The influences of R_O/R_i and W_{GOP} on the TPB of the current sector annular plate structure

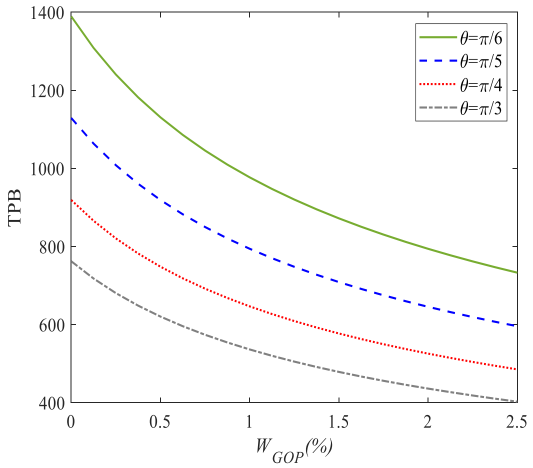

Fig. 19 The influences of sector annular plate's angle and W_{GOP} on the TPB of the current structure

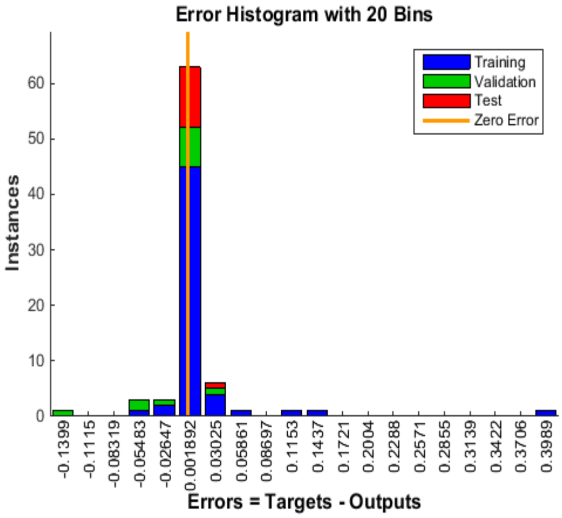

Fig. 20 Instance against error for various training, validations, and tests

This increase at the lower values of W_{GOP} is more clear than higher ones.

Table 3 Regression coefficient and mean squared error (MSE) depending on the number of neurons in the hidden layer

Structure of ANN	Training performance	R	MSE (10^{-4})
12-4-1	25.3273	0.62611	7.4919
12-4-1	6.19034	0.63433	7.14025
12-5-1	6.21654	0.64128	7.5374
12-6-1	6.8874	0.64329	4.92037
12-6-1	4.28753	0.64431	4.02916
12-4-1	4.35403	0.63131	2.0776
12-7-1	4.69027	0.64066	1.30813
12-7-1	0.44818	0.64503	0.99034
12-8-1	0.73184	0.63392	1.03903
12-9-1	0.55874	0.63203	0.94432

The influences of R_O/R_i and W_{GOP} on the TPB of the current sector annular plate structure Fig. 18 is presented. As is seen, by increasing the W_{GOP}, the TPB decreases with different slopes. This issue has been explained in detail in the previous figures. By increasing the R_O/R_i the stiffness of the structure and finally the TPB decreases. This decrease at the lower values of W_{GOP} is more clear than higher ones.

To know about the influences of sector annular plate's angle and W_{GOP} on the TPB of the current structure, Fig. 19 is presented. As is mentioned, by increasing the W_{GOP} the stiffness of the system and finally the TPB decreases. Also, the influence of theta on the TPB is not dependent on the value of W_{GOP} of the reinforcement. As mentioned in the previous figures, by increasing the sector annular plate's angle parameter, the TPB of the structure decreases.

5.3 The presented improved deep neural network's results

During the improved deep neural networks model's development, the collected data is fed in as initial inputs and outputs. Three sets of data are created: one for testing, one for validation, and one for training, totaling seventy percent. The appropriateness of the created model is evaluated using the regression coefficient (R) and mean squared error (MSE). For every data set that is highlighted, the values of R and MSE are shown. The best possible network to minimize Mean Squared Error (MSE) has eleven neurons in its hidden layer. Table 3 presents the findings. The numerical results and the improved deep neural networks model's predictions agree rather well. The natural frequency of laminated composite plates with a cutout is precisely predicted by improved deep neural networks. Regression analysis of the predicted and actual findings is shown in Fig. 20 to assess the efficacy of the suggested model. The regression coefficients (R) that were computed to ascertain the correlation between the values predicted by the improved deep neural networks and those derived from the FE model are shown in Fig. 21. Three separate groups comprise the training, validation, and test datasets. The range of the coefficient R is 0 to 1. The strength of the association rises as R gets closer to one. Table 3's most effective configuration for an artificial neural network is (12-7-1).

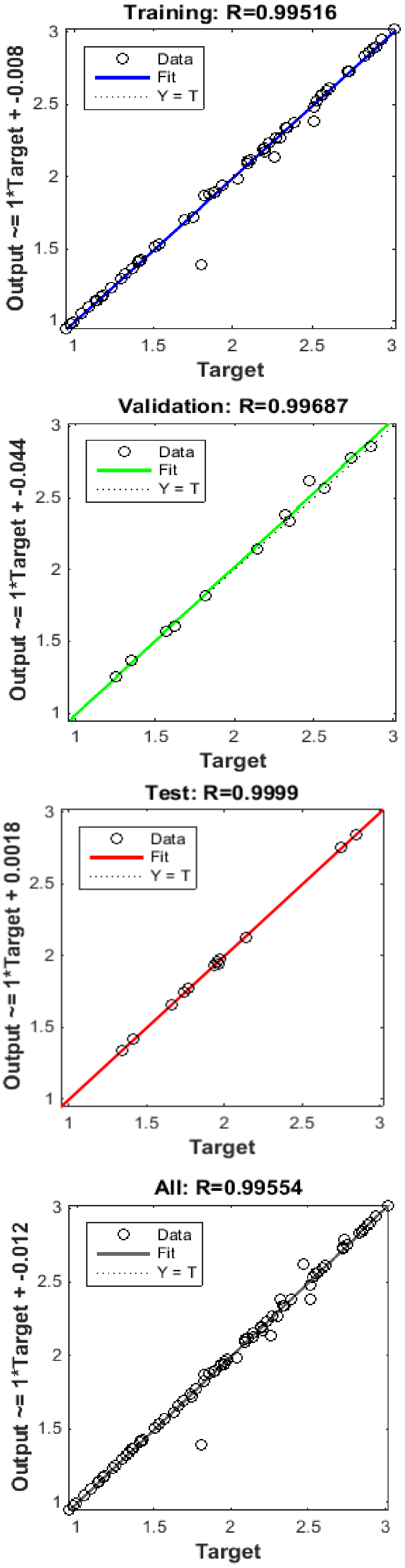

Fig. 21 Output against target for various R parameters

Table 4 adjusting the K_w and W_{GOP} parameters and comparing the dimensionless amplitude of the improved deep neural networks with the numerical simulation results

K_w	W_{GOP}			
	1%		2%	
	Mathematics	Deep Learning	Mathematics	Deep Learning
0	391.704	392.094	416.889	415.455
10^2	424.788	426.774	448.974	443.556
10^3	517.707	521.577	538.917	541.587
10^4	587.889	590.559	601.794	604.767

The findings may be compared with the mathematical simulation results shown in Table 4 by using the designated parameters. The results of the most recent data-driven mathematical modeling, which computed the TPB of the existing composite structure in dimensionless units, are shown in Table 4.

From Table 4 can be concluded that, in the solution strategies outlined, when the K_w and W_{GOP} parameters drop, the amplitude of the current system rises. As W_{GOP} grows, the composite's TPB displayed an annular plate. It is clear from reviewing the data that there is a high degree of agreement between the two approaches.

6. Conclusions

This work examines the behavior of concrete eccentric annular sector plates reinforced with GOPs in terms of thermal post-buckling. Analysis is done on the stability and reaction of the plates under thermal loads using the minimal total potential energy theory. The governing differential equations are effectively solved by the use of the transform differential quadrature technique, while the support conditions are taken into consideration by the Haber-Schaim foundation model. The plates' mechanical characteristics and stability are greatly improved by the incorporation of GOPs, qualifying them for use in cutting-edge engineering applications. The crucial thermal loads and post-buckling trajectories are shown by numerical findings, which provide important new information for the design and optimization of these reinforced structures. This work proposes a machine learning technique that uses datasets obtained from given mathematical models to anticipate complicated engineering occurrences. The system efficiently learns and captures complex patterns from the mathematical models by using machine learning and sophisticated data analytics approaches, resulting in precise and effective forecasts. Using mathematical simulations, the process creates extensive datasets that are utilized to train the machine learning model. With great accuracy, the trained model can forecast a range of engineering outcomes, including strain, stress, and heat reactions. This method allows for quick and accurate analysis by drastically cutting down on the amount of processing time and resources needed for conventional simulations. This all-encompassing method provides a strong foundation for forecasting the thermal post-buckling behavior of reinforced concrete plates, which aids in the creation of durable and effective structural elements for use in civil engineering.

Acknowledgements

This work was supported by Sichuan Province Luzhou city of Stars science and technology planning project(2021-JYJ-100) and (2022-JYJ-130). The authors extend their appreciation to King Saud University for funding this work through Researchers Supporting Project number (RSPD2024R1006), King Saud University, Riyadh, Saudi Arabia.

References

Behravan-Rad, A. and Jafari, M. (2020), "Hygroelasticity analysis of an elastically restrained functionally graded porous metamaterial circular plate resting on an auxetic material circular plate", *Appl. Math. Mech.*, **41**, 1359-1380. https://doi.org/10.1007/s10483-020-2651-7.

Chen, C., Yang, H., Song, K., Liang, D., Zhang, Y. and Ni, J. (2023), "Dissolution feature differences of carbonate rock within hydro-fluctuation belt located in the Three Gorges Reservoir Area", *Eng. Geol.*, **327**, 107362. https://doi.org/10.1016/j.enggeo.2023.107362.

Chen, D., Yang, J. and Kitipornchai, S. (2017), "Nonlinear vibration and postbuckling of functionally graded graphene reinforced porous nanocomposite beams", *Compos. Sci. Technol.*, **142**, 235-245. https://doi.org/10.1016/j.compscitech.2017.02.008.

Chen, J.T., Tsai, M.H. and Liu, C.S. (2009), "Conformal mapping and bipolar coordinate for eccentric Laplace problems", *Comput. Appl. Eng. Educ.*, **17**(3), 314-322. https://doi.org/10.1002/cae.20208.

Dehshahri, K., Nejad, M.Z., Ziaee, S., Niknejad, A. and Hadi, A. (2020), "Free vibrations analysis of arbitrary three-dimensionally FGM nanoplates", *Advances in nano research*. **8**(2), 115-134. https://doi.org/10.12989/anr.2020.8.2.115.

Ebrahimi, F. and Jafari, A. (2017), "Investigating vibration behavior of smart imperfect functionally graded beam subjected to magnetic-electric fields based on refined shear deformation theory", *Adv. Nano Res.*, **5**(4), 281. https://doi.org/10.12989/anr.2017.5.4.281

Ebrahimi, F., Karimiasl, M., Civalek, Ö. and Vinyas, M. (2019a), "Surface effects on scale-dependent vibration behavior of flexoelectric sandwich nanobeams", *Adv. Nano Res.*, **7**(2), 77. https://doi.org/10.12989/anr.2019.7.2.077.

Ebrahimi, F., Karimiasl, M. and Mahesh, V. (2019b), "Vibration analysis of magneto-flexo-electrically actuated porous rotary nanobeams considering thermal effects via nonlocal strain gradient elasticity theory", *Adv. Nano Res.*, **7**(4), 223-231. https://doi.org/10.12989/anr.2019.7.4.223.

Ebrahimi, F. and Salari, E. (2019), "Effect of non-uniform temperature distributions on nonlocal vibration and buckling of inhomogeneous size-dependent beams", *Adv. Nano Res.*, **6**(4), 377. https://doi.org/10.12989/anr.2018.6.4.377

Efraim, E. and Eisenberger, M. (2007), "Exact vibration analysis of variable thickness thick annular isotropic and FGM plates", *J. Sound Vib.*, **299**(4-5), 720-738. https://doi.org/10.1016/j.jsv.2006.06.068.

Ehyaei, J. and Daman, M. (2017), "Free vibration analysis of double walled carbon nanotubes embedded in an elastic medium with initial imperfection", *Adv. Nano Res.*, **5**(2), 179. https://doi.org/10.12989/anr.2017.5.2.179.

Emdadi, M., Mohammadimehr, M. and Navi, B.R. (2019), "Free vibration of an annular sandwich plate with CNTRC facesheets and FG porous cores using Ritz method", *Adv. Nano Res.*, **7**(2), 109. https://doi.org/10.12989/anr.2019.7.2.109

Feng, Y., Mohammadi, M., Wang, L., Rashidi, M. and Mehrabi, P. (2021), "Application of artificial intelligence to evaluate the fresh properties of self-consolidating concrete", *Materials*, **14**(17), 4885. https://doi.org/10.3390/ma14174885.

Firouzianhaji, A., Usefi, N., Samali, B. and Mehrabi, P. (2021), "Shake table testing of standard cold-formed steel storage rack", *Appl. Sci.*, **11**(4), 1821. https://doi.org/10.3390/ma14174885.

Ghannadpour, S. and Moradi, F. (2019), "Nonlocal nonlinear analysis of nano-graphene sheets under compression using semi-Galerkin technique", *Adv. Nano Res.*, **7**(5), 311-324. https://doi.org/10.12989/anr.2019.7.5.311.

Guida-Pietrasanta, F., Boutevin, B., Nuyken, O., Becker, O., Simon, G.P., Dusek, K., Rusanov, A.L., Likhatchev, D., Kostoglodov, P.V. and Müllen, K. (2005), "Polymer-clay nanocomposites", *Inorgan. Polym. Nanocompos. Membr.*, 135-195. https://doi.org/10.1007/b104481.

Han, S., Zheng, D., Mehdizadeh, B., Nasr, E.A., Khandaker, M.U., Salman, M. and Mehrabi, P. (2023a), "Sustainable design of self-consolidating green concrete with partial replacements for cement through neural-network and fuzzy technique", *Sustainability*, **15**(6), 4752. https://doi.org/10.3390/su15064752.

Han, S., Zhu, Z., Mortazavi, M., El-Sherbeeny, A.M. and Mehrabi, P. (2023b), "Analytical assessment of the structural behavior of a specific composite floor system at elevated temperatures using a newly developed hybrid intelligence method", *Buildings*, **13**(3), 799. https://doi.org/10.3390/buildings13030799.

He, X., Ding, J., Habibi, M., Safarpour, H. and Safarpour, M. (2021), "Non-polynomial framework for bending responses of the multi-scale hybrid laminated nanocomposite reinforced circular/annular plate", *Thin Wall. Struct.*, **166**, 108019. https://doi.org/10.1016/j.tws.2021.108019.

He, H., Shuang, E., Ai, L., Wang, X., Yao, J., He, C. and Cheng, B. (2023), "Exploiting machine learning for controlled synthesis of carbon dots-based corrosion inhibitors", *J. Clean. Prod.*, **419**, 138210. https://doi.org/10.1016/j.jclepro.2023.138210.

He, H., Qiao, H., Sun, T., Yang, H. and He, C. (2024a), "Research progress in mechanisms, influence factors and improvement routes of chloride binding for cement composites", *J. Build. Eng.*, 108978. https://doi.org/10.1016/j.jobe.2024.108978.

He, H., Shuang, E., Lu, D., Hu, Y., Yan, C., Shan, H. and He, C. (2024b), "Deciphering size-induced influence of carbon dots on mechanical performance of cement composites", *Constr. Build. Mater.*, **425**, 136030. https://doi.org/10.1016/j.conbuildmat.2024.136030.

He, L., Maalla, A., Zhou, X. and Tang, H. (2024c), "Buckling and post-buckling of anisogrid lattice-core sandwich plates with nanocomposite skins", *Thin Wall. Struct.*, **199**, 111828. https://doi.org/10.1016/j.tws.2024.111828.

Horne, J., Beddingfield, E., Knapp, M., Mitchell, S., Crawford, L., Mills, S.B., Wrist, A., Zhang, S. and Summers, R.M. (2020), "Caffeine and theophylline inhibit β-galactosidase activity and reduce expression in Escherichia coli", *ACS omega*, **5**(50), 32250-32255. https://doi.org/10.1021/acsomega.0c03909

Hu, D., Sun, H., Mehrabi, P., Ali, Y.A. and Al-Razgan, M. (2023), "Application of artificial intelligence technique in optimization and prediction of the stability of the walls against wind loads in building design", *Mech. Adv. Mater. Struct.*, 1-18. https://doi.org/10.1080/15376494.2023.2206208.

Huang, H., Huang, M., Zhang, W., Pospisil, S. and Wu, T. (2020), "Experimental investigation on rehabilitation of corroded RC columns with BSP and HPFL under combined loadings", *J. Struct. Eng.*, **146**(8), 04020157. https://doi.org/10.1061/(ASCE)ST.1943-541X.0002725.

Huang, H., Huang, M., Zhang, W. and Yang, S. (2021), "Experimental study of predamaged columns strengthened by HPFL and BSP under combined load cases", *Struct. Infrastruct. Eng.*, **17**(9), 1210-1227. https://doi.org/10.1177/13694332221131153.

Huang, H., Li, M., Zhang, W. and Yuan, Y. (2022), "Seismic behavior of a friction-type artificial plastic hinge for the precast beam–column connection", *Arch. Civil Mech. Eng.*, **22**(4), 201. https://doi.org/10.1007/s43452-022-00526-1.

Huang, H., Yao, Y., Liang, C. and Ye, Y. (2022), "Experimental study on cyclic performance of steel-hollow core partially encased composite spliced frame beam", *Soil Dyn. Earthq. Eng.*, **163**, 107499. https://doi.org/10.1016/j.soildyn.2022.107499.

Huang, H., Yuan, Y., Zhang, W. and Zhu, L. (2021), "Property assessment of high-performance concrete containing three types of fibers", *Int. J. Concr. Struct. Mater.*, **15**(1), 1-17. https://doi.org/10.1186/s40069-021-00476-7.

Javani, M., Kiani, Y. and Eslami, M. (2020), "Thermal buckling of FG graphene platelet reinforced composite annular sector plates", *Thin Wall. Struct.*, **148**, 106589. https://doi.org/10.1016/j.tws.2019.106589.

Kong, G., Sun, G., Liu, H. and Li, J. (2021), "Dynamic response of ballastless track XCC pile-raft foundation under train axle loads", *J. Test. Evaluat.*, **49**(3), 1691-1704. https://doi.org/10.1520/JTE20180032.

Kumar, B.R. (2018), "Investigation on mechanical vibration of double-walled carbon nanotubes with inter-tube Van der waals forces", *Adv. Nano Res.*, **6**(2), 135. https://doi.org/10.12989/anr.2018.6.2.135

Li, H., Yang, Y., Wang, X. and Tang, H. (2023), "Effects of the position and chloride-induced corrosion of strand on bonding behavior between the steel strand and concrete", *Structures*, 2023. https://doi.org/10.1016/j.istruc.2023.105500

Li, Z., Gao, M., Lei, Z., Tong, L., Sun, J., Wang, Y., Wang, X. and Jiang, X. (2023), "Ternary cementless composite based on red mud, ultra-fine fly ash, and GGBS: Synergistic utilization and geopolymerization mechanism", *Case Stud. Constr. Mater.*, **19**, e02410. https://doi.org/10.1016/j.cscm.2023.e02410.

Liew, K., Yang, J. and Kitipornchai, S. (2003), "Postbuckling of piezoelectric FGM plates subject to thermo-electro-mechanical loading", *Int. J. Solids Struct.*, **40**(15), 3869-3892. https://doi.org/10.1016/S0020-7683(03)00096-9.

Liu, B., Yang, H. and Karekal, S. (2020), "Effect of water content on argillization of mudstone during the tunnelling process", *Rock Mech. Rock Eng.*, **53**, 799-813. https://doi.org/10.1007/s00603-019-01947-w.

Liu, J., Mohammadi, M., Zhan, Y., Zheng, P., Rashidi, M. and Mehrabi, P. (2021), "Utilizing artificial intelligence to predict the superplasticizer demand of self-consolidating concrete incorporating pumice, slag, and fly ash powders", *Materials*, **14**(22), 6792. https://doi.org/10.3390/ma14226792.

Lu, D., Wang, G., Du, X. and Wang, Y. (2017), "A nonlinear dynamic uniaxial strength criterion that considers the ultimate dynamic strength of concrete", *Int. J. Impact Eng.*, **103**, 124-137. https://doi.org/10.1016/j.ijimpeng.2017.01.011.

Lu, D., Zhou, X., Du, X. and Wang, G. (2019), "A 3D fractional elastoplastic constitutive model for concrete material", *Int. J. Solids Struct.*, **165**, 160-175. https://doi.org/10.1016/j.ijsolstr.2019.02.004.

Luo, Y., Liao, P., Pan, R., Zou, J. and Zhou, X. (2024), "Effect of bar diameter on bond performance of helically ribbed GFRP bar to UHPC", *J. Build. Eng.*, **91**, 109577. https://doi.org/10.1016/j.jobe.2024.109577.

Mehrabi, P., Honarbari, S., Rafiei, S., Jahandari, S. and Alizadeh Bidgoli, M. (2021), "Seismic response prediction of FRC rectangular columns using intelligent fuzzy-based hybrid metaheuristic techniques", *J. Ambient Intell. Human. Comput.*, **12**, 10105-10123. https://doi.org/10.3390/ma14174885.

Mehrabi, P., Shariati, M., Kabirifar, K., Jarrah, M., Rasekh, H., Trung, N.T., Shariati, A. and Jahandari, S. (2021), "Effect of pumice powder and nano-clay on the strength and permeability of fiber-reinforced pervious concrete incorporating recycled concrete aggregate", *Constr. Building Mater.*, **287**, 122652. https://doi.org/10.3390/ma14174885.

Mock, M.B., Zhang, S., Pakulski, K., Hutchison, C., Kapperman, M., Dreischarf, T. and Summers, R.M. (2024), "Production of 1-methylxanthine via the biodegradation of theophylline by an optimized Escherichia coli strain", *J. Biotechnol.*, **379**, 25-32. https://doi.org/10.1016/j.jbiotec.2023.11.005

Mock, M.B., Zhang, S., Pniak, B., Belt, N., Witherspoon, M. and Summers, R.M. (2021), "Substrate promiscuity of the NdmCDE N7-demethylase enzyme complex", *Biotechnol. Notes*, **2**, 18-25. https://doi.org/10.1016/j.biotno.2021.05.001

Pang, B., Jin, Z., Zhang, Y., Xu, L., Li, M., Wang, C., Zhang, Y., Yang, Y., Zhao, P. and Bi, J. (2022), "Ultraductile waterborne epoxy-concrete composite repair material: Epoxy-fiber synergistic effect on flexural and tensile performance", *Cement Concr. Compos.*, **129**, 104463. https://doi.org/10.1016/j.cemconcomp.2022.104463.

Qiu, Y. (2019), "Estimation of tail risk measures in finance: Approaches to extreme value mixture modeling", Johns Hopkins University.

Qiu, Y. and Wang, J. (2024). "A machine learning approach to credit card customer segmentation for economic stability", *Proceedings of the 4th International Conference on Economic Management and Big Data Applications*, ICEMBDA 2023, October 27-29, 2023, Tianjin, China, 2024.

Sadd, M.H. (2009), *Elasticity: Theory, Applications and Numerics*, Academic Press.

Salari, F.E.E. (2016), "Thermal loading effects on electro-mechanical vibration behavior of piezoelectrically actuated inhomogeneous size-dependent Timoshenko nanobeams", *Adv. Nano Res.*, **4**(3), 197. https://doi.org/10.12989/anr.2016.4.3.197

Song, K., Yang, H., Liang, D., Chen, L. and Jaboyedoff, M. (2024), "Step-like displacement prediction and failure mechanism analysis of slow-moving reservoir landslide", *J. Hydrol.*, **628**, 130588. https://doi.org/10.1016/j.jhydrol.2023.130588.

Sun, L., Wang, C., Zhang, C., Yang, Z., Li, C. and Qiao, P. (2023), "Experimental investigation on the bond performance of sea sand coral concrete with FRP bar reinforcement for marine environments", *Adv. Struct. Eng.*, **26**(3), 533-546. https://doi.org/10.1177/13694332221131153.

Taheri, E., Firouzianhaji, A., Mehrabi, P., Vosough Hosseini, B. and Samali, B. (2020), "Experimental and numerical investigation of a method for strengthening cold-formed steel profiles in bending", *Appl. Sci.*, **10**(11), 3855. https://doi.org/10.3390/app10113855.

Taheri, E., Firouzianhaji, A., Usefi, N., Mehrabi, P., Ronagh, H. and Samali, B. (2019), "Investigation of a method for strengthening perforated cold-formed steel profiles under compression loads", *Appl. Sci.*, **9**(23), 5085. https://doi.org/10.3390/ma14174885.

Taheri, E., Mehrabi, P., Rafiei, S. and Samali, B. (2021), "Numerical evaluation of the upright columns with partial reinforcement along with the utilisation of neural networks with combining feature-selection method to predict the load and displacement", *Appl. Sci.*, **11**(22), 11056. https://doi.org/10.3390/app112211056.

Tian, J., Wang, B., Guo, R., Wang, Z., Cao, K. and Wang, X. (2021), "Adversarial attacks and defenses for deep-learning-based unmanned aerial vehicles", *IEEE Internet Things J.*, **9**(22), 22399-22409. https://doi.org/10.1109/JIOT.2021.3111024.

Toghroli, A., Mehrabi, P., Shariati, M., Trung, N.T., Jahandari, S. and Rasekh, H. (2020), "Evaluating the use of recycled concrete aggregate and pozzolanic additives in fiber-reinforced pervious concrete with industrial and recycled fibers", *Constr. Build. Mater.*, **252**, 118997. https://doi.org/10.3390/ma14174885.

Tounsi, A., Benguediab, S., Semmah, A. and Zidour, M. (2013), "Nonlocal effects on thermal buckling properties of double-walled carbon nanotubes", *Adv. Nano Res.*, **1**(1), 1. https://doi.org/10.12989/anr.2013.1.1.001

Wei, J., Ying, H., Yang, Y., Zhang, W., Yuan, H. and Zhou, J. (2023), "Seismic performance of concrete-filled steel tubular composite columns with ultra high performance concrete plates", *Eng. Struct.*, **278**, 115500. https://doi.org/10.1016/j.engstruct.2022.115500.

Wu, C.P., Chen, Y.H., Hong, Z.L. and Lin, C.H. (2018), "Nonlinear vibration analysis of an embedded multi-walled carbon nanotube", *Adv. Nano Res.*, **6**(2), 163. https://doi.org/10.12989/anr.2018.6.2.163

Wu, J., Yang, Y., Mehrabi, P. and Nasr, E.A. (2023), "Efficient machine-learning algorithm applied to predict the transient shock reaction of the elastic structure partially rested on the viscoelastic substrate", *Mech. Adv. Mater. Struct.*, 1-25. https://doi.org/10.1080/15376494.2023.2183289.

Wu, Y., Wang, X., Fan, Y., Shi, J., Luo, C. and Wang, X. (2024), "A study on the ultimate span of a concrete-filled steel tube arch bridge", *Buildings*, **14**(4), 896. https://doi.org/10.3390/buildings14040896.

Xia, D., Alexander, A.K., Isbell, A., Zhang, S., Ou, J. and Liu, X.M. (2017), "Establishing a co-culture system for Clostridium cellulovorans and Clostridium aceticum for high efficiency biomass transformation", *J. Sci. Heal. Univ. Ala.*, **14**, 8-13.

Yang, H., Chen, C., Ni, J. and Karekal, S. (2023), "A hyperspectral evaluation approach for quantifying salt-induced weathering of sandstone", *Sci. Total Environ.*, **885**, 163886. https://doi.org/10.1016/j.scitotenv.2023.163886.

Yang, H., Ni, J., Chen, C. and Chen, Y. (2023), "Weathering assessment approach for building sandstone using hyperspectral imaging technique", *Heritage Sci.*, **11**(1), 70. https://doi.org/10.1186/s40494-023-00914-7.

Yang, H., Song, K. and Zhou, J. (2022), "Automated recognition model of geomechanical information based on operational data of tunneling boring machines", *Rock Mech. Rock Eng.*, 1-18. https://doi.org/10.1007/s00603-021-02723-5.

Yao, X., Lyu, X., Sun, J., Wang, B., Wang, Y., Yang, M., Wei, Y., Elchalakani, M., Li, D. and Wang, X. (2023), "AI-based performance prediction for 3D-printed concrete considering anisotropy and steam curing condition", *Constr. Build. Mater.*, **375** 130898. https://doi.org/10.1016/j.conbuildmat.2023.130898.

Zhang, Z., Li, Y., Wu, H., Zhang, H., Wu, H., Jiang, S. and Chai, G. (2020), "Mechanical analysis of functionally graded graphene oxide-reinforced composite beams based on the first-order shear deformation theory", *Mech. Adv. Mater. Struct.*, **27**(1), 3-11. https://doi.org/10.1080/15376494.2018.1444216.

Zhu, X., Lu, Z., Wang, Z., Xue, L. and Ebrahimi-Mamaghani, A. (2020), "Vibration of spinning functionally graded nanotubes conveying fluid", *Eng. Comput.*, 1-22. https://doi.org/10.1007/s00366-020-01123-7

CC